universität wien

DIPLOMARBEIT / DIPLOMA THESIS

Titel der Diplomarbeit / Title of the Diploma Thesis

„Broadband Reflectance and Transmittance Characterization of Crystalline Supermirrors”

verfasst von / submitted by

Lukas Perner

angestrebter akademischer Grad / in partial fulfilment of the requirements for the degree of

Magister der Naturwissenschaften (Mag. rer. nat.)

Wien, 2019 / Vienna, 2019

Studienkennzahl lt. Studienblatt / degree programme code as it appears on the student record sheet:	A 190 333 412
Studienrichtung lt. Studienblatt / degree programme as it appears on the student record sheet:	UF Deutsch, UF Physik
Betreut von / Supervisor:	Dipl.-Phys. Dr. Oliver H. Heckl

Table of contents

Acknowledgments

First and foremost, I thank my supervisors Oliver Heckl and Georg Winkler at the Christian Doppler Laboratory for Mid-IR Spectroscopy and Semiconductor Optics (CDL Mid-IR) for their abundance of patience, which I know I taxed at one point or another during my lab work and while writing this thesis. Their ongoing advice and resourcefulness were a huge source of knowledge and I am thankful for all the help I got, from both them and the other group members, Aline Mayer and Jakob Fellinger.

In addition, I forward my thanks to the Laboratory's business partner Crystalline Mirror Solutions (CMS) for providing the cavity mirrors used during this project, as well as the joint effort on the mirror characterization measurements. Especially, I gratefully acknowledge Dominic Bachmann's continuous effort and help, both in the lab and as a key contact between CMS and the CDL Mid-IR.

Furthermore, I wish to thank all those fellow students, whom I have shared the countless hours of learning. Be it in lecture halls, seminar rooms, or the lab – especially, Florian Brandt, Josef Huber, and Thomas Wurm have been companions for the better part of my academic career.

Moreover, I want to express my gratitude to Melanie Lette, who has, mostly patiently, endured my long working hours and supported me during the last exams.

Finally, I am particularly grateful for the support, both financial and moral, my parents, Betina Strasser and Wolfgang Perner, have accorded to me. Without their ongoing encouragement, I could not have mastered my studies.

1 Introduction

1.1 State of Research

Ever since high-reflectivity dielectric coatings became available in the visible (VIS) range in the 1980s, it was also necessary to precisely and accurately measure the characteristics of such mirrors. Consequently, experimental schemes to measure mirror reflectance R independent of light source intensity fluctuations were developed. These approaches are the so called cavity ring-down (CRD) setups, measuring the so-called cavity decay time τ directly (with a reflectance resolution as low as 5ppm) [1]. This method is based on a technique published four years earlier, obtaining the decay time by a measurement of the cavity-induced phase shift of an intensity modulated source laser [2].

As the ring-down time does also depend on intracavity losses (e.g., gas absorption), CRD schemes were subsequently used in spectroscopy experiments with great success (with [3] commonly accepted as the first in this series; a historical overview on CRD spectroscopy is given in [4, pp. 3–12]).

With the advancements in high-reflectivity coatings and laser technology, extending applications to the near infrared (NIR) regime, came experiments demonstrating CRD experiments utilizing broadband Fabry-Pérot diode lasers at different wavelengths [5]–[7]. In the course of these measurements, optical feedback of the ring-down cavity on the source laser was observed. This effect (already described for V-shaped and Brewster angle cavities by Romanini et. al. in combination with distributed feedback (DFB) and extended cavity diode lasers) was either suppressed [5] or used for a better signal to noise ratio [6] in reflectance measurements.

Many materials and technologies used to manufacture supermirrors in the VIS and NIR regimes cannot be transferred to the mid infrared (MIR) regime without major complications. Among other reasons, this is due to the fact that many optical materials become lossy or even opaque in the MIR regime [8]. As a result, it was only in

recent years that mirror reflectance in the MIR regime approached unity (e.g., 99.97% at 3300 nm and 99.92% for crystalline coatings [8]).

Whereas broadband NIR diode lasers used in previous CRD experiments exhibit a typical effective linewidth of approximately 3 nm [5], [6], typical genuine MIR Fabry-Pérot diode lasers, i.e. quantum cascade lasers (QCLs) and interband cascade lasers (ICLs), exhibit a spectrum spanning several tens of nanometers (see A 2.1). This lead previous efforts in the field of MIR CRD reflectometers to utilize frequency-shifted NIR sources, e.g. optical frequency combs shifted to MIR wavelengths using an optical parametric oscillator [8], [9]. This approach is also superior to small linewidth MIR DFB sources due to its tuning range, comb structure, stability and beam quality.

1.2 Aims of the Thesis

As already noted by Anderson in 1984 [1], mirror reflectance R varies greatly, even for mirrors of (almost) identical specifications. What was true for coatings mirrors in the VIS range then, is true for MIR supermirror coatings today. This is due to intrinsic uncertainties involved in the production process [8]; e.g. long growth times compared to shorter-wavelength mirrors, as coating thickness increases with wavelength (see 2.4). Especially for high-precision applications (e.g. the aforementioned CRD spectroscopy), it is therefore often necessary to perform precise, yet simple and reliable, measurements of basic mirror properties (this being reflectance R, transmittance T and residual losses$l$) for each individual mirror.

The thesis at hand aims to demonstrate the feasibility of such measurements for state-of-the-art crystalline mirror coatings in the MIR range with a cost-effective apparatus. This is of equal interest for both manufacturers (offering characterization as a service) and research groups (providing them with a cost- and space-effective setup). Additionally, the mirror pair used in this setup is one of the first of its kind at a wavelength above 4 µm, demonstrating the advancements of mirror technology, constantly pushing to higher wavelengths.

For this purpose, two setups were built. On the one hand, a CRD reflectometer using a MIR QCL source was designed. On the other hand, a simple direct transmittance measurement approach is implemented. This was feasible using a lock-in amplifier employing a white light source.

All this was done with the additional goal of using robust, inexpensive, commercially available components. Additionally, the measurement uncertainties should be on par with more expensive solutions, and significantly smaller than the projected total loss (combined transmittance, absorbance, and scatter loss) of current super mirror technology.

2 Basics and Theory

Most CRD experiments make use of open resonators, i.e. two facing reflective surfaces without a waveguide in between (see 2.2). When these surfaces are spherically curved, the fitting solution for the resonant electrical field are so called Gaussian waves (see 2.1). Since many lasers are, in principle, also open resonators with an active medium, they often emit approximately Gaussian beams. Additionally, state-of-the-art supermirror coatings are so-called DBR stacks (explained in 2.4), they work just as well if illuminated from the back.

2.1 Gaussian Beams

Gaussian waves are paraxial, i.e. they have a well-defined direction of propagation and exhibit a relatively small divergence. Therefore they are often called Gaussian beams [10, p. 195]. As a paraxial wave, the Gaussian beam must be a solution to the Helmholtz equation

$$\left(\nabla^2 + k^2\right)U(r) = 0 \tag{1}$$

which is obtained by substituting the complex representation of the wavefunction

$$U(r,t) = U(r)e^{i\omega t} \tag{2}$$

into the well-known wave equation

$$\left(\nabla^2 - \frac{1}{c^2}\frac{\partial^2}{\partial t^2}\right)U = 0 \tag{3}$$

where ∇^2 is the Laplacian Operator in three dimensions and $c = c_0/n$ is the speed of light in a homogenous medium [11, pp. 45–46]. Herewith, I further introduced the wavenumber k and angular frequency ω which are related to the wavelength λ and frequency f by

$$k = \frac{\omega}{c} = \frac{2\pi}{\lambda} = \frac{2\pi f}{c} \tag{4}$$

Defining the z-axis as the direction of propagation, the complex wavefunction $U(r)$ takes the form

$$U(r) = A(r)e^{-ikz} \tag{5}$$

where the paraxial approximation demands that the envelope $A(r)$ changes slowly with λ, so that the wavefront normals are approximately parallel to the z-Axis (i.e., there is a well-defined direction of propagation) for small changes in z (i.e. negligible divergence). Since that means $\partial_z \ll kA$ and $\partial_z^2 \ll k^2 A$, the Helmholtz Equation approximates to

$$\left(\frac{\partial^2}{\partial x^2} + \frac{\partial^2}{\partial y^2} - 2ik\frac{\partial}{\partial z}\right)A(r) = 0 \tag{6}$$

Solving this equation for a paraboloidal wave and then shifting the solution by a constant iz_r gives the complex envelope $A(r)$ of the Gaussian beam

$$A(r) = \frac{A_i}{q(z)}e^{-ik\frac{\rho^2}{2q(z)}} \tag{7}$$

where $\rho^2 = x^2 + y^2$ and

$$q(z) = z + iz_r \tag{8}$$

is the complex beam parameter and $z_r \in \mathbb{R}$ is called the Rayleigh range [11, pp. 81–82]. The complex beam parameter $q(z)$ is related to the real parameters $R(z)$ and $w(z)$, identified as beam radius of curvature (ROC) and beam width, respectively, by the equation

$$\frac{1}{q(z)} = \frac{1}{R(z)} - i\frac{\lambda}{\pi w^2(z)} \tag{9}$$

Substituting (9) and (7) into (5) gives an expression for the complex amplitude

$$U(\rho, z) = A_0 \frac{w_0}{w(z)}\exp\left(-\frac{\rho^2}{w^2(z)}\right)\exp\left(-i\left(kz + k\frac{\rho^2}{2R(z)} - \varphi_G\right)\right) \tag{10}$$

where $\varphi_G = \tan^{-1}(z/z_r)$ is called the Gouy-phase. Note that (10) gives $U(\rho, z)$ as a function of real, i.e. measurable, parameters: First, the beam waist

$$w_0 = \frac{w(z)}{\sqrt{1 + \left(z/z_r\right)^2}} \tag{11}$$

which is the minimum diameter of the Gaussian beam, located at $z = 0$. Secondly, the ROC is given by

$$R(z) = z\left[1 + \left(\frac{z_r}{z}\right)^2\right] \tag{12}$$

Since $R = \infty$ at $z = 0$, the phase front is plane at the beam waist position. Lastly, the Rayleigh range is given by

$$z_R = \frac{\pi w_0^2}{\lambda} \tag{13}$$

To emphasize the paraxial nature of the Gaussian beam, $U(\rho, z)$ is given as a function of radial distance ρ and axial distance z rather than r (see Figure 1). This is especially useful in experiment: Regularly, beam properties are measured at fixed values of z, then deriving more fundamental parameters (e.g., the beam waist w_0).

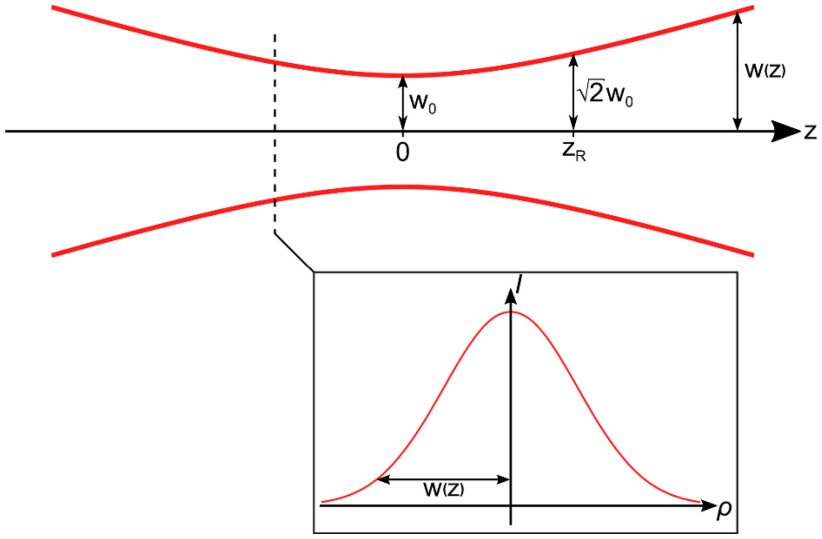

Figure 1: The main illustration shows the $w(z)$ contour line of a Gaussian beam propagating in the z-direction. Also labeled are the minimum beam diameter $w_0 = w(z = 0)$ and the Rayleigh range z_R. The inset shows the transverse beam profile at some arbitrary z-position, which exhibits the characteristic Gaussian profile. Denoted in both schematics is the beam waist $w(z)$. From the inset it is obvious, that only part of the beam intensity is inside the beam waist.

For large z (i.e. $z \gg z_R$) we derive from (11) the relation

$$w(z) \approx \frac{w_0}{z_0} z = \theta_0 z \tag{14}$$

where θ_0 is the divergence half-angle [12, p. 80]. This angle describes the beam divergence of the Gaussian beam as it propagates far away from z_0, where the divergence behaves linearly with z as can be seen from (14).

Equipped with the complex amplitude of the Gaussian beam (10) the optical intensity is given as

$$I(\rho,z)=\left|U(r)\right|^2=I_0\left(\frac{w_0}{w(z)}\right)^2\exp\left(-\frac{2\rho^2}{w^2(z)}\right) \tag{15}$$

where $I_0 = |A_0|^2$ is introduced for convenience [11, p. 83]. From (15) the beam power can be derived by integration over a transverse plane at arbitrary and fixed axial position by

$$P=\int_0^\infty I(\rho,z)2\pi\rho\,\mathrm{d}\rho=\frac{I_0}{2}\left(w_0^2\pi\right) \tag{16}$$

The total optical power is therefore half the peak intensity I_0 times the "beam area" [11, p. 85]. Rewriting (15) in terms of P gives

$$I(\rho,z)=\frac{2P}{w^2(z)\pi}\exp\left(\frac{2\rho^2}{w^2(z)}\right) \tag{17}$$

and therefore, the share of power inside an area of radius ρ_0 is

$$\frac{P_{in\rho_0}}{P}=1-\exp\left(-\frac{2\rho_0^2}{w^2(z)}\right) \tag{18}$$

where $P_{\mathrm{in}\rho}$ is obtained as in (16), simply integrating from 0 to ρ_0 instead [11, p. 85]. It is of note, that the "beam area", or any circle with radius $\rho_0 = \mathrm{w}(z)$, only contains about 86.5% of the total beam power. This is of some importance when dealing with optical components, such as mirrors or lenses, and critical when building ultra-low-loss optical resonators with 'small' mirrors (i.e. mirrors, whose area is comparable to the 'beam area' at the location of the mirror), as beam clipping upon reflection can lead to substantial power loss.

Of course, beams emitted by real lasers are often not perfectly Gaussian. For example, diode lasers often exhibit ellipticity. However, one can maintain the Gaussian description by analyzing a real beam in more than one axis and by introducing additional parameters. The most common and basic correction to the Gaussian model

is given by the introduction of the M^2 parameter, also called beam quality factor. This factor is introduced to all the above formulas by defining the divergence half-angle as

$$\theta_0 = M^2 \frac{\lambda}{\pi w_0} \tag{19}$$

instead of the definition given in (14). This essentially introduces a measure of 'Gaussianness' to the description of real laser beams observed in experiment: A value of $M^2 = 1$ corresponds to a perfectly Gaussian beam, while $M^2 > 1$ for all other beam shapes. As will be derived in 2.2.2, spherical mirror resonators only accept Gaussian beams, so M^2 is also a measure for the part of beam intensity one can hope to couple into an optical cavity on resonance.

2.2 Optical Resonators

There are many different types of optical resonators or cavities.[1] However, their main purpose is to amplify light of certain wavelengths λ by meeting resonance conditions. Furthermore, the underlying principle is always the same: Light is confined inside a structure of highly reflective surfaces to be reflected many times inside the resonator. This includes so-called closed resonators of different geometries (e.g. box-shaped), which confine light regardless of its direction of propagation. A simpler form are open resonators: These only confine light along a certain direction of propagation.

The simplest model for such an open resonator is two parallel and plane facing mirrors in presence of a plane wave propagating back and forth between them (see 2.2.1). However, as already mentioned in 2.1, most coherent sources exhibit a quasi-Gaussian beam profile. Therefore, 2.2.2 treats the theory on spherical mirror resonators, which are more suitable in conjunction with the output of laser sources.

2.2.1 Plane-Wave Plane Mirror Resonator

A simple plane mirror resonator consists of two facing, flat (and, for now, ideal) mirrors, separated by a distance d, which are both parallel, to the z–axis. On the other hand, a plane wave propagating in the z direction is described by its complex amplitude

[1] The terms "resonator" and "cavity" are used interchangeably in this thesis.

$$U(z) = A\exp(-ikz) \tag{20}$$

with a complex constant A. Looking at the phase $\arg(U(z))$, one finds that the wavefronts are perpendicular to the z–axis and separated from each other by a wavelength $\lambda = 2\pi/k$ [11, p. 47].

Inside the optical cavity, however, the original plane wave (20) will consequently be reflected from both mirrors. This also means, that interference occurs. For this interference to be constructive, the wave must be self-reproducing, i.e. both direction $\pm z$ and phase $\varphi = kz$ must be the same after a round-trip inside the cavity. While the first condition, reproduction of direction, is trivially met for the given resonator, the second condition, phase reproduction, imposes an important condition: Since the mirror reflections contribute a phase shift of π each per round-trip, or, in total, the phase shift due to the round-trip distance $2d$ must fulfil

$$\varphi = k2d = q2\pi \quad q \in \mathbb{N} \tag{21}$$

for the wave to be self-reproducing [11, p. 314]. From that, using (4), one finds that the so-called resonant longitudinal modes of an optical cavity are given by

$$f_q = q\frac{c}{2d} \tag{22}$$

and the spacing between two such resonant modes, called the free spectral range, is

$$f_{FSR} = f_{q+1} - f_q = \frac{c}{2d} \tag{23}$$

This important result is also illustrated in Figure 2. Note that the condition is very strict, with resonance only occurring at the exact frequency of the associated resonant longitudinal mode.

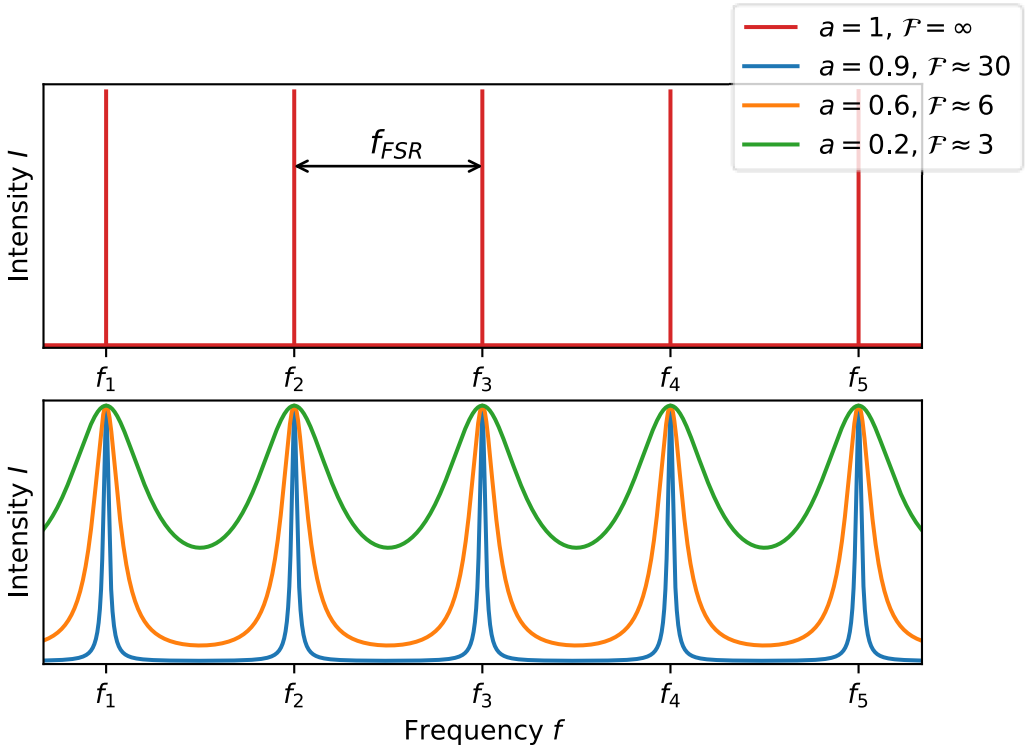

Figure 2: Intesity response function for a lossless resonator (top) and resonators with different loss factors a (bottom).

For a plane wave inside this resonator we can now reach the following conclusion [11, p. 315]: Starting with a plane wave U_0 of the form (20), one round-trip results in another wave U_1. As already discussed, U_1 must be identical to U_0 except for a round-trip phase shift of $\varphi = k2d$, i.e. $U_1 = e^{-i\varphi}U_0$. This process repeats for each round-trip, adding another wave $U_q = e^{-iq\varphi}U_0$ to the superposition. The resulting wave is therefore described by the complex amplitude

$$U = \sum_{q=0}^{\infty} U_q \tag{24}$$

with the magnitude $|U_q|$ being the same for every q, since the resonator is, by definition, lossless. As noted above, this will result in a buildup of power inside the cavity, only if (21) is exactly met.

Introducing losses to the resonator changes this situation: Again, starting with a complex amplitude U_0, the complex amplitude U_1 gets a round-trip phase added. However, now U_1 is also attenuated by a factor a, so

$$U_1 = ae^{-i\varphi}U_0 = hU_0 \tag{25}$$

Combining this with (24) one obtains

$$U = \sum_{q=0}^{\infty} h^q U_0 = U_0 \frac{1}{1-h} \tag{26}$$

since factoring out U_0 gives a geometric series in h. From that, one can calculate the spectral intensity response

$$I(f) = |U|^2 = \frac{I_0 / (1-a)^2}{1 + (2\mathcal{F}/\pi)^2 \sin^2(\pi f / f_{FSR})} \tag{27}$$

in dependence on f (for a given resonator of length d with an attenuation factor a, see Figure 2), with $I_0 = |U_0|^2$ [11, pp. 316–317]. Here, the important quantity

$$\mathcal{F} = \frac{\pi\sqrt{a}}{1-a} \tag{28}$$

called the cavity finesse, was introduced. Relation (27) is called the spectral response of a two mirror resonator. Comparing this function with the results in (21)–(23), one can observe the following: First, the spacing between two peaks in (27) is still given by the free spectral range (23). Secondly, the larger the finesse $\mathcal{F}$, the closer a lossy resonator resembles an ideal, i.e. lossless, cavity. Lastly, the lower the finesse $\mathcal{F}$, the broader is the FWHM Δf of the peaks in (27). This relation can be expressed as [11, p. 72,318]

$$\Delta f \approx \frac{f_{FSR}}{\mathcal{F}} \quad \text{if } \mathcal{F} \gg 1 \tag{29}$$

These facts are illustrated in Figure 2 and bear some importance for experimental implementations: As soon as resonators have losses, resonances do not only occur at the exact value of a longitudinal mode, but in a spectral region according to (29).

Having shown the effects of resonator losses, we now move to their sources [11, p. 318]: On the one hand, loss is introduced by absorption and scatter in the medium inside the cavity. This introduces an attenuation of $\exp(-2\alpha_m d)$, with α_m being the material-dependent absorption coefficient. On the other hand, there are loss mechanisms involving the individual cavity mirrors. In opposition to the reflectance per mirror R, the sum of all mirror losses is called total loss L. This total loss can be further discriminated by the involved mechanism: Transmittance T (which is often desirable to some extent, see [8]), absorption A and residual loss S. There are two

important contributors to S: Scatter and the fact that real mirrors have a limited aperture, whereas waves or beams, are, in principle, infinite (which led to (18)). As both A and S are nonrecoverable losses, they are often combined as residual loss l. Due to energy conservation this gives rise to the relation

$$R + \underbrace{T + \underbrace{A + S}_{l}}_{L} = 1 \tag{30}$$

For the round-trip attenuation of the intensity inside the two-mirror cavity, this nets to

$$a^2 = R_1 R_2 e^{-2\alpha_m d} \tag{31}$$

where R_1 and R_2 are the reflectances of the individual cavity mirrors and α_m is the absorption coefficient of the medium inside the cavity. Assuming $\alpha_m \ll 1$ and $R_{1,2} \approx 1$, the finesse (28) can therefore be expressed as

$$\mathcal{F} \approx \frac{\pi}{\left(1 - \frac{R_1 + R_2}{2}\right) + d\alpha_m} \tag{32}$$

Hence, the finesse is inversely proportional to the total cavity losses [1]. Since $(R_1 + R_2)/2$ is exactly the mean reflectance $\bar{R}$, (32) simplifies to

$$\mathcal{F} \approx \frac{\pi}{\bar{L} + d\alpha_m} \tag{33}$$

Therefore, the finesse $\mathcal{F}$ can be directly related to the total losses $L = T + A + S$ of a single cavity mirror, if the cavity is built of two identical mirrors [1]. Of course, (33) further simplifies in the case of negligible intra-cavity absorption, i.e. if $\alpha_m \ll \bar{L}$ (e.g., in vacuum). Successively, the mean mirror losses are inversely proportional to the finesse $\mathcal{F}$.

Although all the above holds, for a flat mirror cavity to form a resonator, the two mirrors must be exactly parallel, to each other and to the wave fronts. Otherwise, the wave would exhibit a parallel misalignment after each round-trip. This means that flat mirror resonators are highly sensitive to misalignment and therefore impractical in real-world experiments [11, p. 327].

2.2.2 Spherical Mirror Resonators

As briefly mentioned at the beginning of this chapter, real lasers often emit (approximately) Gaussian beams. As (10) and (12) have shown, a Gaussian beam's wave fronts (i.e., planes of equal phase) are spherically curved. In particular, (10) gives the phase of a Gaussian beam as

$$\varphi(\rho,z)=kz+k\frac{\rho^2}{2R(z)}-\varphi_G \tag{34}$$

which includes the second term, dependent on the transverse distance ρ. Hence, in general, a reflection from a flat mirror would impose a phase shift. In addition, the beam would not be refocused: Instead, according to (18), most of the Gaussian beam's power would leak out of the cavity on each reflection, due to the beam's divergence. Only a resonator comprised of spherical mirrors allows for the confinement of a Gaussian beam, i.e. the Gaussian beam is a mode of the spherical mirror resonator.

The critical condition for confinement is that the two mirror's radii of curvature (ROC) match the beam's ROC at their respective positions [11, p. 332], i.e.

$$\begin{aligned} R_1 &= R(z_1) \\ -R_2 &= R(z_2) \end{aligned} \tag{35}$$

where R_i is the ROC of the mirrors located at z_1 and

$$z_2 = z_1 + d \tag{36}$$

The minus sign for R_2 arises from the fact that the sign of $R(z)$ is dependent on the mirror location ($R(z) < 0$ for $z < 0$), while the sign of R_i is instead dependent on the mirror geometry ($R_i < 0$ for concave mirrors).[2] Using (12), it follows from (35)–(36) that

$$z_r^2 = \frac{-d(R_1+d)(R_2+d)(R_1+R_2+d)}{(R_1+R_2+2d)^2} \tag{37}$$

Since z_r is real, i.e. $z_r^2 > 0$, from that we also get the expression

[2] In other words: Since the two mirrors of a simple resonator will always face each other, one of the mirror coordinate systems, used to define the mirror's ROC (concave vs. convex), will always be laterally inverted with respect to the coordinate system defined for the beam.

$$0 \leq \left(1+\frac{d}{R_1}\right)\left(1+\frac{d}{R_2}\right) \leq 1 \tag{38}$$

called the stability condition (see Figure 3) [11, p. 333], [13, p. 1314]. This relation is of prime importance for the construction of real cavities, since it defines stable resonator lengths d for two mirrors with given ROCs R_1 and R_2.

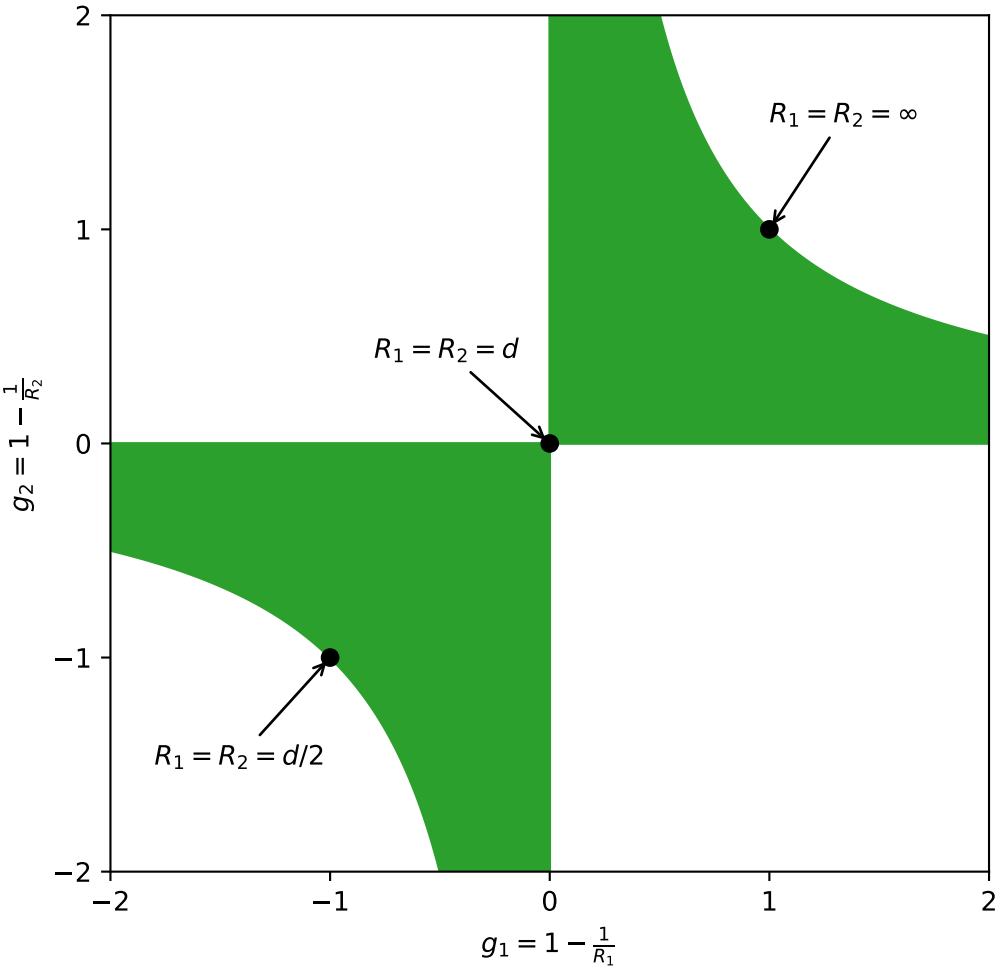

Figure 3: Stability diagram for a two-mirror resonator. Stable configurations are inside the green area. Some configurations with $R_1 = R_2$ have been highlighted.

As indicated by (33), when measuring mirror properties, one often uses (nearly) identical mirrors [1]. This means, that both mirrors must be concave with $R_1 = R_2$.

We have now ensured that the Gaussian beam shape retraces itself after a single round-trip, i.e. that a light wave described by (10) is confined, if (38) holds.

However, as shown for plane waves in 2.2.1, a resonant mode must also retrace the phase. In contrast to (20), the axial part of the Gaussian phase

$$\varphi(0,z) = kz - \varphi_G \tag{39}$$

is retarded by the Gouy phase φ_G compared to a plane wave. This results in a round-trip phase shift of $2kd - \left(\varphi_G(z_2) - \varphi_G(z_1)\right)$ and, by means of (21), in the resonance frequencies

$$f_q = qf_{FSR} + \frac{\varphi_G(z_2) - \varphi_G(z_1)}{\pi} f_{FSR} \tag{40}$$

where the free spectral range between two adjacent longitudinal modes is identical to that of a planar mirror resonator of the same length with the resonances being shifted corresponding to the second term in (40).

2.2.3 Transverse Modes

For each longitudinal mode, sets of so-called transverse modes exists. This arises from the fact, that the Gaussian beam is not the only solution for (6). In fact, the Gaussian beam is fundamental to two complete orthogonal sets of solutions [11, pp. 100–104], [13, pp. 1316–1317].

The first set of solutions, called the Hermite-Gaussian modes, is obtained by trying a more general solution for (6) by modulating the complex envelope of the Gaussian solution along the transverse Cartesian coordinates x and y, i.e. making the separation ansatz

$$A(x,y,z) = g\left(\sqrt{2}\frac{x}{W(z)}\right) h\left(\sqrt{2}\frac{y}{W(z)}\right) \exp\left(if(z)\right) A_G(\rho,z) \tag{41}$$

where A_G is the complex envelope obtained in (7). Solving (6) for (41) leads to the solution

$$\begin{aligned} U_{l,m}(x,y,z) = A_{l,m}\left(\frac{w_0}{w(z)}\right) H_l\left(\sqrt{2}\frac{x}{w(z)}\right) H_m\left(\sqrt{2}\frac{y}{w(z)}\right) \exp\left(-\frac{\rho^2}{w^2(z)}\right) \\ \exp\left(-i\left(kz + k\frac{\rho^2}{2R(z)} - (l+m+1)\varphi_G\right)\right) \end{aligned} \tag{42}$$

where $l, m \in \mathbb{N}^0$, $A_{l,m}$ is a constant, and $H_n(u) = (-1)^n e^{u^2}\left(d^n e^{-u^2}/du^n\right)$ is the Hermite polynomial of order n [11, pp. 100–102], [14, p. 491]. The solution for $l = m =$

0 is identical to (10), whereas for higher orders of l and m, also called TEM_{lm} modes, more complex transverse intensity distributions arise.

Although the Hermite-Gaussian modes form a complete set of solutions, i.e. every solution can be written as a superposition of Hermite-Gaussian modes, there is another family of solutions, called the Laguerre-Gaussian modes, which is also a complete and orthogonal set [15]. The Laguerre-Gaussian solution is obtained by rewriting the paraxial Helmholtz equation (6) in cylindrical coordinates and using the separation of variables in (ρ, φ, z) to get the solution

$$U_{l,m}(\rho,\varphi,z) = A_{l,m}\left(\frac{w_0}{w(z)}\right)\left(\frac{\rho}{w(z)}\right)^{l} L_{l,m}\left(\frac{2\rho^2}{w^2(z)}\right)\exp\left(-\frac{\rho^2}{w^2(z)}\right) \exp\left(-i\left(kz + k\frac{\rho^2}{2R(z)} + l - (l+2m+1)\varphi_G\right)\right) \tag{43}$$

where $l, m \in \mathbb{N}^0$, $A_{l,m}$ is a constant, and $L_{l,m}(u) = (e^u u^{-l}/m!)(d^m u^{l+m} e^{-u}/du^m)$ is the associated Laguerre polynomial of order l, m [14, pp. 491–492]. Again, the solution for $l = m = 0$ corresponds to the fundamental Gaussian beam.

When comparing (42) and (43) with the fundamental Gaussian solution (10) there are some important observations: First, $R(z)$ remains unchanged, regardless of the transverse mode numbers l, m; i.e. the confinement condition is the same for all transverse modes associated with a longitudinal mode f_q. In principle, this allows for the coexistence of several higher order modes in a resonator. Secondly, inspecting the phase terms, one can see that the Gouy phase φ_G is multiplied by a factor dependent on the mode numbers l, m, effectively shifting the resonance to higher frequencies by a small amount. Lastly, the higher the mode number, the larger is the transverse area with substantial power. Hence, for higher order modes to be excited, the resonator mirror's aperture must be larger. Otherwise, the fundamental Gaussian beam will resonate best, since it has the lowest losses [14, p. 492].

2.3 Cavity Ring-Down Reflectometers

As already indicated in 2.2.1, the cavity finesse $\mathcal{F}$ can be directly related to the losses L of a single cavity mirror. This result, obtained in (33), already suggests that a resonator consisting of two identical mirrors could be used as a reflectometer, since $L = 1 - R$.

As discussed in 2.2, when light is fed into a Fabry-Pérot cavity from a coherent source, a significant field will build up only when it is on (or near) a cavity resonance frequency. Since both cavity mirrors exhibit a transmittance, T_1 and T_2, respectively, a certain fraction of the intracavity intensity I, given in (27), will be transmitted through each cavity mirror. We can relate the intensity transmitted through the second mirror to the intracavity intensity by

$$I_{\text{trans}} = T_2 I \tag{44}$$

where T_2 is the mirror's transmittance. On the other hand, the intensity I_{in} of the light incident on the first cavity mirror is only related to the intensity I_0 by

$$I_0 = T_1 I_{\text{in}} \tag{45}$$

since all further contributions to the intracavity field result from reflections of I_0 inside the cavity, as shown in (24)–(26). Consequently, the cavity transmittance is given by

$$T_{\text{cav}} = \frac{I_{\text{trans}}}{I_{\text{in}}} = T_1 T_2 \frac{I}{I_0} = \frac{\dfrac{T_1 T_2}{(1-a)^2}}{1 + \left(2\mathcal{F}/\pi\right)^2 \sin^2\left(\pi f / f_{FSR}\right)} \tag{46}$$

and therefore, directly proportional to the intra-cavity intensity I [11, pp. 321–322]. This means, that we can measure the intensity of the field leaking out of the cavity to obtain information about cavity characteristics. However, from (46), we can also see that such a direct measurement is dependent on the stability of I_{in} and therefore not feasible when the fluctuation is on or above the same order of magnitude as the loss factor a, as is the case with highly reflective mirrors.

However, another measurement approach, called cavity ring-down (CRD) scheme, can be used in such cases. Suppose that at some instant in time t_{off} a significant field intensity I_{off} has built up inside the cavity. If we now switch off the incoming intensity I_{in} very fast, the transmitted intensity $I_{\text{trans}}(t)$ for $t > t_{\text{off}}$ is not given by the steady-state solution in (46), but by the transient response of the cavity. This response, however, is determined by an exponential decay with a constant τ, which is determined by the round-trip cavity losses and the cavity length [1].

The exact derivation of intensity decay formula, given in full by [1], [16], and partially in [4, pp. 16–17], shall be omitted here, as we won't need any of the

intermediate results. However, we will justify the results in an approach that relies on these derivations. In the scenario of rapid laser shutoff at t_{off}, the transmitted intensity for times $t > t_{\text{off}}$ is well-described by the formula

$$I_{\text{trans}}(t) = I_{\text{off}} e^{-t/\tau} \tag{47}$$

where I_{off} is the intensity at t_{off}. Relating the round-trip attenuation factor (31) to the round-trip time

$$t_r = \frac{2d}{c} \tag{48}$$

we get, for the attenuation after n round trips

$$I_{\text{off}} e^{-\frac{2nL}{c\tau}} = I_{\text{off}} a^{2n} \tag{49}$$

since only the intensity attenuation due to cavity parameters can influence the system [17, p. 357]. Therefore, the time constant τ, called ring-down time or decay time, is defined by

$$\tau = \frac{d}{c} \ln\left(\frac{1}{a}\right) \approx \frac{d}{c(1-a)} \tag{50}$$

where the approximation holds for $a \approx 1$. The ring-down time is therefore also connected to the finesse by

$$\mathcal{F} = \frac{\pi c}{d} \tau \tag{51}$$

Consequently, and according to (32), the decay time is linked to the mean mirror reflectance $\bar{R}$ by

$$\bar{R} = 1 - \bar{L} = 1 - \left(\frac{d}{c\tau} + d\alpha_m\right) \tag{52}$$

As the time trace is recorded as the voltage V_{trans} of a photodiode in experiment, we must account for a possible offset voltage V_{offset}, resulting in the model

$$V(t) = V_{\text{off}} e^{-\frac{t}{\tau}} + V_{\text{offset}} \tag{53}$$

when determining τ directly from an oscilloscope trace.

It should be emphasized here, that the CRD method is therefore independent of both fluctuations in the source laser, used to excite a cavity resonance, and detector absolute intensity calibration. Furthermore, the decay time τ is longer, the lower the cavity losses. Therefore, the better the mirrors we want to characterize by means of (52), the lower the demands on the setup in terms of response time (e.g. detector response). However, the setup response can be a limiting factor when using the single exponential model (53), as is shown in [18].

2.4 Distributed Bragg Reflectors

State of the art highly reflective coatings are most commonly designed as Distributed Bragg Reflectors (DBR), also called Bragg/DBR stacks, illustrated in Figure 4. These are stacks of alternating layers of high- and low-index dielectric optical materials. This index contrast causes a partial reflection of light waves/beams at each layer boundary.

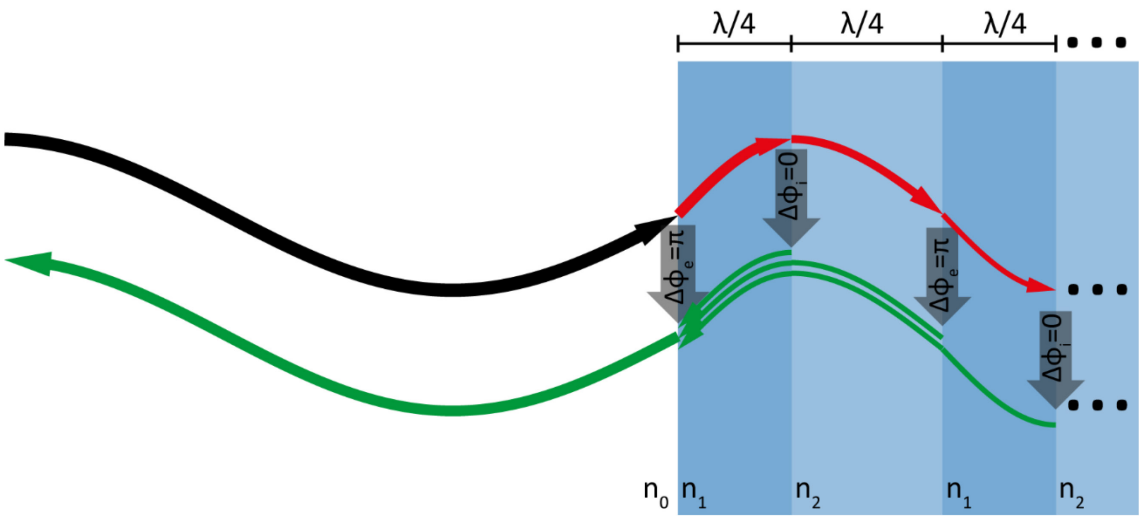

Figure 4: Working principle of a DBR mirror at normal incidence. Shown are the first 1.5 periods of a DBR mirror. The incoming lightwave (black) is partially transmitted (red) and reflected (green) at each interface between different media with refractive indices $n_1 = 1.5n_2 = 2n_0$. At interfaces where the originating medium has a lower refractive index, external refraction occurs, and the reflected wave experiences a phase shift of $\Delta\varphi_e = \pi$. In the inverse case, internal reflection occurs, not adding a phase shift, i.e. $\Delta\varphi_i = 0$. Since the DBR stack is composed of layers with $\lambda_{n_0}/4n_i$ thickness, this leads to constructive interference of the incoming and all reflected waves.

2.4.1 Basic Properties of Bragg Mirrors

Assuming locally planar reflection (i.e. the reflecting surface is parallel to the impinging light beam wave front at every point), normal incidence is ensured. The reflectance is therefore polarization-independent in this case. We start with a simple

DBR layout: A stack consisting of 1.5 periods, i.e. a single layer of high-index material followed by a single layer of low-index material, and again a high-index layer surrounded by air (compare Figure 4).

For such a DBR stack to be highly reflective at a certain wavelength, the reflected wave needs to interfere constructively with the incoming wave; i.e., for the phase difference,

$$\varphi_r - \varphi_0 = \Delta\varphi \overset{!}{=} 2\pi \tag{54}$$

We assume $n_1 > n_2 > n_0$. Therefore, at the first boundary (air to high-index)

$$\varphi_{r1} = \pi \tag{55}$$

The transmitted part of the incident wave passes into the high-index medium, therefore picking up a phase shift dependent on twice the optical width

$$D_1 = n_1 d_1 \tag{56}$$

of the layer. As internal reflection ($n_1 > n_2$) does not contribute to the phase shift, the total phase shift for the part reflected at the boundary to the low-index material is

$$\varphi_{r2} = 2kd_1 n_1 \tag{57}$$

Where k is the wave vector (which is a scalar in this case). The next reflection occurs at the boundary low- to high-index, therefore external reflection ($n_2 < n_1$) occurs. In this case, there is an additional phase shift of π upon reflection, amounting to a total phase shift of

$$\varphi_{r3} = 2kn_1 d_1 + 2kn_2 d_2 + \pi \tag{58}$$

compared to the wave reflected directly off the surface. For constructive interference to occur among these reflected waves

$$\varphi_{r1} = \varphi_{r2} = \varphi_{r3} \tag{59}$$

must hold. From condition (59) follows $D_1 = D_2 = \lambda_{\text{center}}/4$ and, more general,

$$D_n = \frac{\lambda_{\text{center}}}{4} \tag{60}$$

if low- and high-index is strictly alternated. This is true, because the phase shift of reflections off further stacks solely result in additional phase shifts of the same form as (57) and (58).

On the other hand, the amplitude reflection and transmission coefficients for a single reflection off a non-lossy, nonmagnetic, dielectric material are given by [12, p. 211]

$$r_{12} = \frac{n_1 - n_2}{n_1 + n_2} \tag{61}$$

and

$$t_{12} = 1 - r_{12} = \frac{2n_2}{n_1 + n_2} \tag{62}$$

respectively, for both s- and p-polarized light (if normal incidence is maintained).

The corresponding single boundary reflectance R is given by

$$R = |r|^2 = \left(\frac{n_1 - n_2}{n_1 + n_2} \right)^2 \tag{63}$$

and it follows from energy conservation that

$$T = 1 - R \tag{64}$$

in the absence of residual loss, i.e. if $l = A + S = 0$, in agreement with (30).

Assuming (60), the power reflectance of an N–periodic DBR surrounded by a single medium is consequently given by

$$R = \left(\frac{n_1 - n_2}{n_1 + n_2} \right)^{4N} \tag{65}$$

It should be emphasized that this formula only gives the maximum reflectance of a given DBR stack. This maximum is located at the design wavelength defined by the layer thickness. However, DBRs exhibit a bandgap, i.e. a region of high reflectivity located around this maximum. More precise mirror designs are therefore often done numerically.

2.4.2 Transfer Matrix Modelling of DBR Mirrors

To calculate the reflectance spectrum of a multi-layered medium, such as DBR structures, transmission matrix formalism is the most straightforward approach. Instead of the travelling wave approach employed in 2.2, summing up all the attenuated reflections, we now model the structure as a matrix product and impose correct boundary conditions. The result is the steady state solution without the need to track all individual reflections [12, p. 246].

The model for a paraxial optical structure (e.g. a system of lenses, mirrors, and/or slabs) can be modelled as follows: The light is represented by the respective wavefunctions of two plane waves travelling to the right and to the left. The superposition of these two waves is given by

$$U = U_1 + V_1 = u_1 \exp(-ikz) + v_1 (ikz) \tag{66}$$

On the other hand, the propagation through the optical system is represented by the operation [19, p. 6]

$$\begin{pmatrix} u_0 \\ v_0 \end{pmatrix} = M \begin{pmatrix} u_T \\ v_T \end{pmatrix} \tag{67}$$

where M, called transfer or transmission matrix, is a 2×2 matrix representing the action of the optical system on the wave. This matrix M is usually the product of matrices, where a single matrix represents a single component of the optical system (e.g. a boundary between two materials, propagation through a thin lens).

Imposing the correct boundary conditions, this can be used to determine the amplitude reflectance and transmittance of a paraxial optical system. In the case of a DBR structure, b_0 at the left of the optical structure is the complex amplitude of all left-travelling (i.e. reflected) waves combined, i.e. the amplitude reflectance r. Since there is no light source to the right of the structure, $u_T = 1 - r = t$ (from (62)) and $v_T = 0$ (as all left travelling waves stem from reflection). In terms of (67), these boundary conditions can be expressed as [19, p. 7]

$$\begin{pmatrix} 1 \\ r \end{pmatrix} = M \begin{pmatrix} t \\ 0 \end{pmatrix} \tag{68}$$

Fundamentally, a DBR structure consists layers of material of refractive index n_i and thickness d_i and the boundary surfaces between these layers. The transfer matrix for a layer of homogenous, non-lossy dielectric material is given by

$$M_{n_a} = \begin{pmatrix} e^{-ikn_a d_a} & 0 \\ 0 & e^{-ikn_a d_a} \end{pmatrix} \tag{69}$$

as can be justified by the discussion in 2.4.1, whereas the transfer matrix for planar reflection (normal incidence) is given by

$$M_{12} = \begin{pmatrix} 1 & r_{12} \\ r_{12} & 1 \end{pmatrix} = \begin{pmatrix} 1 & \frac{n_1 - n_2}{n_1 + n_2} \\ \frac{n_1 - n_2}{n_1 + n_2} & 1 \end{pmatrix} \tag{70}$$

Therefore, a $N.5$ period DBR with light incident from the left is modelled by the equation

$$\begin{pmatrix} 1 \\ r \end{pmatrix} = M_{n_0} M_{01} \underbrace{M_{n_1} M_{12} M_{n_2} M_{21} \cdots M_{n_1} M_{12} M_{n_2} M_{21}}_{N \text{ times}} M_{n_1} M_{1T} M_{n_T} \begin{pmatrix} t \\ 0 \end{pmatrix} \tag{71}$$

where M_{n_0} and M_{n_T} are matrices of the form (69) for the initial and terminal medium surrounding the DBR structure (in most cases this would be air and/or some optical substrate) and $n_1 > n_2$. Naturally, we assume that (60) holds for all M_{n_a}, so that the DBR is a highly reflective mirror around λ_{center}.

3 Experimental Setup and Results

In the following chapter, the results of our measurements are presented and analyzed. In 3.1, we describe the cavity mirrors, present Fourier transform infrared spectrometer (FTIRS) measurements of the individual mirrors and develop a 'mean-mirror' model to compare to the cavity ring-down (CRD) measurements. The CRD measurements themselves, as well as the used setup, are described in 3.2. There, we also discuss the influence of intra-cavity gas absorption, leading to a correction for the CRD results. Finally, in 3.3, the direct transmission measurements, performed with a single mirror, are shown and discussed.

3.1 Crystalline Mirror Design

The crystalline mirrors (serial numbers CMS1032 and CMS1033[3]) characterized in this thesis were grown by CMS in a single coating run. These mirrors are designed as a 34.5 period DBR stack (see 2.4) of alternating GaAs and $Al_{0.92}Ga_{0.08}As$ layers with a design central wavelength of 4.5 µm and a diameter of 8 mm. These DBR stacks were afterwards transferred to super-polished Si substrates with an ROC of 1 m (for details on the substrate transfer process see [20]) and a diameter of 1". The transmittance spectrum of the original mirror design, on which the parameters for the growth process were based, is show in Figure 5.

After the growth process an X-ray microscope measurement was performed by the manufacturer. This measurement indicated that the DBR structure was slightly thicker, i.e. the center transmission wavelength was shifted towards higher wavelengths by about 1%.

3.1.1 FTIRS Measurements of the Mirror Pair

Due to the above-mentioned indications of deviations in the growth process, FTIRS measurements of the individual mirrors provided to us by CMS were conducted. For these transmittance measurements of the mirror specimen, a commercial FTIRS

[3] More precisely, the substrates are serial numbered. It is therefore possible, that other coatings will be bonded to these substrates in the future.

(Bruker Vertex 80) was used. Measurements of the mirrors were taken in a nitrogen flooded environment to minimize excess losses due to gas absorption. The results of these measurements are shown in Figure 5. As can be seen from the plot, precise loss measurements below ~200 ppm are not feasible.

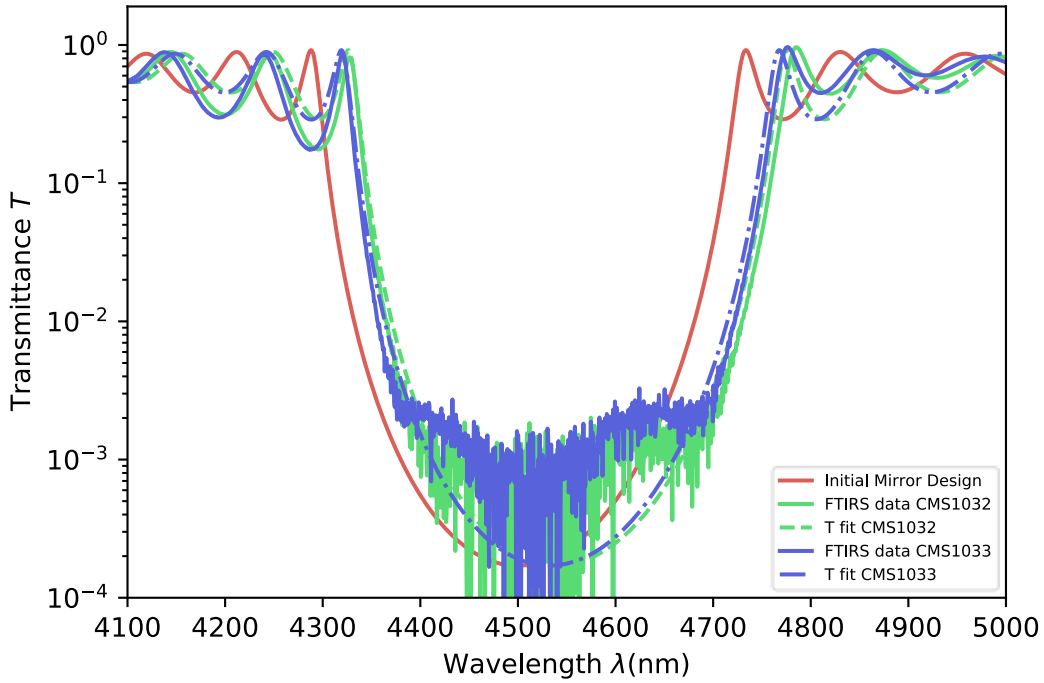

Figure 5: FTIRS traces for CMS1032 (solid green line) and CMS1033 (solid blue line), alongside the initial mirror design (red line). The systematic shift of the mirror stopbands towards higher wavelengths is confirmed. Also shown are the best fit curves of the transfer matrix model for CMS1032 and CMS1033 (dashed green and blue lines, respectively).

However, this measurement is useful to determine the center wavelength of the mirrors CMS1032 and CMS1033 more accurately. For this purpose, a model for the total transmittance T was developed based on (71).[4] This model assumes, that each individual layer is of a constant $\lambda_{\text{center}}/4$ thickness and that there was no deviation from the $Al_{0.92}Ga_{0.08}As$ alloy ratio (which would result in a different index of refraction for the lower-index layers). These assumptions are plausible, since parameters are held constant during the coating growth process. In other words, it is highly likely that all deviations from the original design are small systematic inaccuracies rather than tolerance-driven imprecisions.

[4] For the Python 3 implementation of this optimization routine, the tmm package was used. This package for transfer matrix calculations is described by its creator in [19].

This assumption was confirmed by the best fit of the aforementioned model to the FTIRS measurements for the individual mirrors. These best fit curves are also shown in Figure 5. The fitted parameter, the stopband center wavelength, is given by

$$\lambda_{\text{center,1032}} = (4540.40 \pm 0.10)\,\text{nm}$$

and

$$\lambda_{\text{center,1033}} = (4532.55 \pm 0.10)\,\text{nm}$$

for mirrors CMS1032 and CMS1033, respectively. This corresponds to a shift of mirror center wavelength by 0.9% and 0.7% towards higher wavelengths, supporting the assumption of a systematic deviation from the originally projected λ_{design} of 4500 µm by less than 1%.

Data on the layers respective refractive indices were taken from [21], [22] for GaAs, from CMS for $Al_{0.92}Ga_{0.08}As$ and [23], [24] for Si, while the refractive index of air was approximated as $n_{\text{air}} \approx 1$.

The fitted model did not include free parameters for absorption losses in the DBR layers. This is because the transmission spectrum of a DBR stack is much less influenced by additional absorption losses than the reflectance spectrum.

Furthermore, the signal-to-noise ratio of the FTIRS method deteriorates below 300 ppm, leading to a measurement uncertainty surpassing the expected mirror losses. This results in noisy data, which can be seen from the measurement data in Figure 5.

Due to these reasons, neither absorption coefficients can be reliably fitted to the FTIRS data, nor can mirror reflectance be measured precisely by the FTIRS method.

3.1.2 Correction of the Mirror Model

Since the fitted values presented in 3.1.1 are shown to be shifted from the initial design, a new model to compare to the ring-down measurements is developed.

For that purpose, the pointwise arithmetic mean of the two fit curves obtained in 3.1.1 is taken to obtain the transmittance curve of a 'mean mirror'. This approach is superior to a model that assumes a single mirror with center wavelength $(\lambda_{\text{center,1032}} + \lambda_{\text{center,1033}})/2$. Such a simple model would deviate from the expected

ring-down cavity results in stopband width and minimal transmittance at the stopband center, as can be seen from (30) and (32).

In contrast, the ring-down time depends on the mean of the cavity mirrors' reflectivity, as can be seen from (52). This makes the 'pointwise mean mirror' model, also shown in Figure 6, the ideal model for comparison to ring-down reflectance measurements.

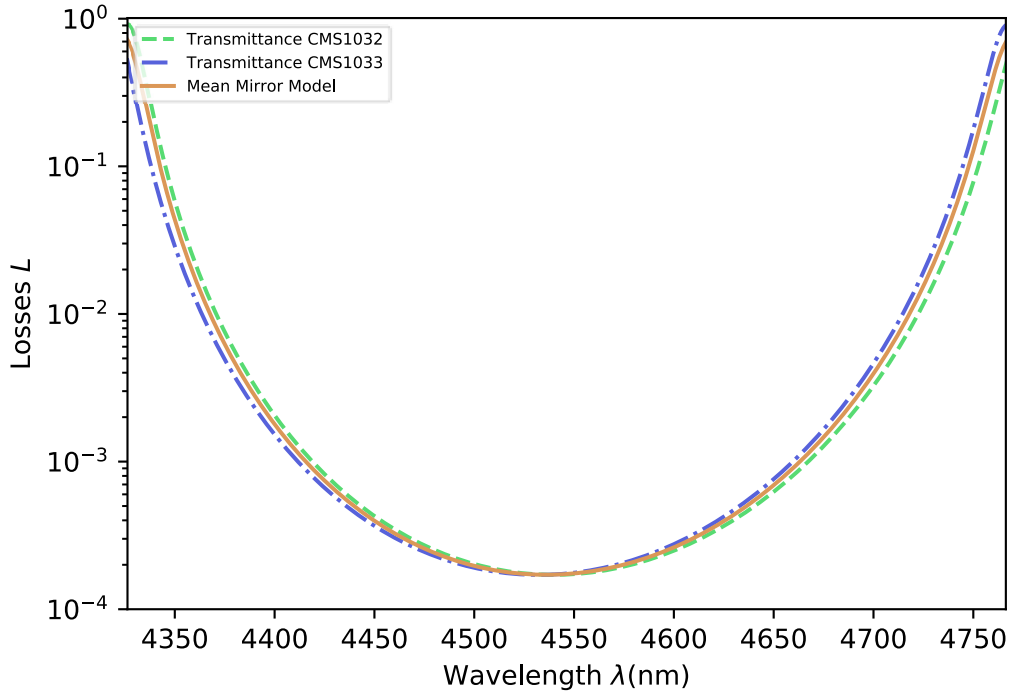

Figure 6: Loss model for comparison to CRD measurements. Shown are the best fit curves for CMS1032 (dashed green line) and CMS1033 (dashed blue line) alongside the resulting mean mirror model (solid orange line). Compared to Figure 5, only the stopband center is shown, so that the difference between the curves is visible.

From this model we expect a mean mirror total loss of

$$\bar{L}(\lambda_{\text{center}} = 4536\,\text{nm}) \approx 171.2\,\text{ppm}$$

in the limit of negligible residual loss, i.e. $l = A + S \approx 0$.

3.2 Reflectance Measurements

Based on the theory in 2.3, a cavity ring-down reflectometer was built from the mirrors described in 3.1. The setup is shown in Figure 7, whereas the parts are described in detail in 3.2.1. The measurement results obtained with this setup are presented in 3.2.4.

3.2.1 Cavity Ring-Down Setup

The cavity ring-down setup consisted of three main parts (compare Figure 7): First, the laser source and beam shaping; secondly, the measurement cavity (itself consisting of the highly reflective mirror pair); thirdly, the measurement apparatus.

The laser source is a commercially available Fabry-Pérot QCL diode (TL QF4550CM1, see A 2.1), mounted in a C-mount laser mount (TL LDMC20) and powered by a QCL current and TEC controller (TL ITC4002QCL). The emitted beam is collimated by an aspheric lens (TL C037TME-E) mounted directly to the laser mount. Subsequently, the collimated output is redirected to a retroreflector, which is used to tune the length of the beam path, followed by a mode-matching telescope, consisting of two concave lenses with focal lengths 40 mm and 50 mm (TL LA5370-E and TL LA5763-E). For ease of alignment, a HeNe gas laser (Melles Griot, $\lambda = 632.8$ nm) was overlapped with the QCL beam.

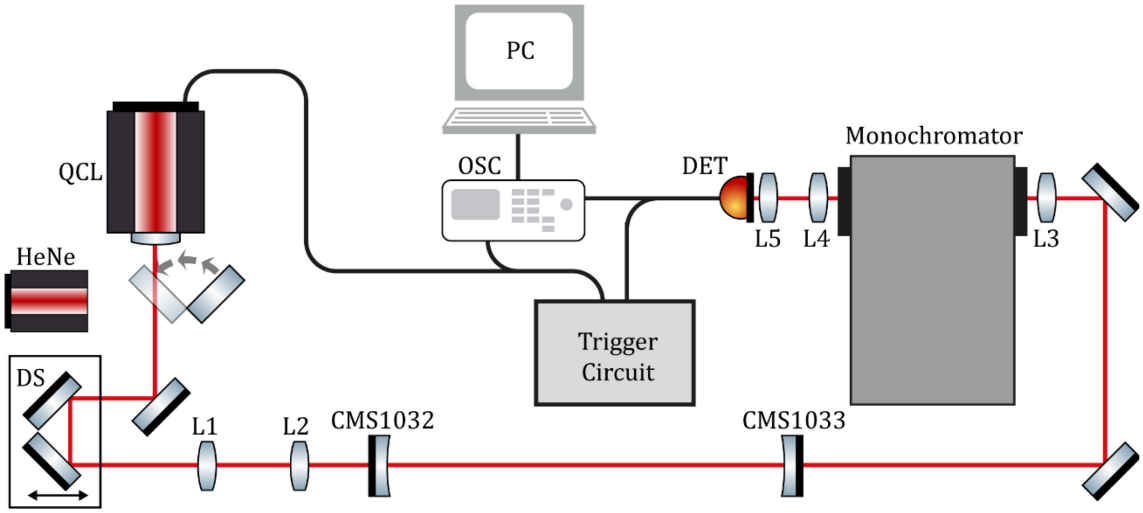

Figure 7: Schematic of the CRD setup. Following the beam path, the apparatus consisted of: A QCL diode laser with controller unit (omitted), the delay-stage (DS) for light path length tuning, mode matching lenses L1 and L2, the measurement cavity consisting of the mirror pair CMS1032 and CMS1033, a monochromator with focusing lenses L3 and L4 and a detector (DET), also with a focusing lens L5. The detector is connected to both an oscilloscope (OSC) and a trigger circuit. The circuit is used to rapidly shut off the QCL and trigger a ring-down measurement on the OSC when the signal surpasses a predefined threshold. The measurement is then processed by a PC. (Illustration created with component library three by Alexander Franzen)

The measurement cavity itself is built from the mirror pair CMS1032 and CMS1033, described in detail in 3.1. The cavity length was chosen as

$$d = (92.0 \pm 0.1)\text{cm}$$

From that and the mirror's ROC the resonant modes of the cavity could be derived, and the mode-matching telescope was adjusted to shape the collimated laser beam accordingly. We also ascertained, that the beam diameter at the cavity mirrors' location was much smaller than the mirror coating diameter. Therefore losses according to (18) could be excluded. Furthermore, we ensured single TEM_{00} mode excitation of the measurement cavity by means of a microbolometer camera.

The acquisition apparatus is situated right behind the cavity. The first part is a reflection grating monochromator (Spectral Products CM110, see A 3). It was used to spectrally filter the light transmitted by the measurement cavity by means of a grating with 300 G/mm and a blaze wavelength of $\lambda_B = 2500$ nm. This was necessary to determine the mirror reflectance in a narrow wavelength range. Since slits of width 300 µm were used for all measurements, the bandpass of the monochromator λ_{BP} is between 2.8 nm and 3.0 nm, dependent on the center wavelength of transmission (manufacturer's specifications). Together with the specified wavelength precision and accuracy $\Delta\lambda_{\mathrm{spec}} = \pm 0.7$ nm (see A 3) this amounts to a total uncertainty of $\Delta\lambda = \Delta\lambda_{\mathrm{spec}} + \lambda_{BP}/2$ between 3.5 nm and 3.7 nm for wavelength measurements in our ring-down experiment. To minimize beam clipping at the entrance slit of the monochromator, the beam was focused on the slit with a lens (focal length 40 mm, TL LA5370-E) and then recollimated behind the monochromator with an identical lens.

The beam was then focused (lens of focal length 20 mm, TL LA5315-E) on an amplified, AC-coupled InAsSb detector (TL PDA10PT-EC, see A 2.3), connected to both an oscilloscope (Tektronix TBS2104) and a trigger circuit. The oscilloscope is, in turn, connected to a PC for automated acquisition.

The trigger circuit (see A 1 for schematic) is connected to the oscilloscope and the laser diode controller. It is used to monitor the signal measured by the detector. As soon as this monitor signal reaches a predefined threshold, the trigger circuit sends a signal to both the laser diode controller and the oscilloscope, rapidly switching off the laser and triggering the acquisition of the ring-down signal.

3.2.2 Optical Feedback

As the cavity is aligned on resonance, a feedback effect on the Fabry-Pérot QCL can be observed. This effect leads to strong resonances, with much higher cavity transmission than the expected steady-state baseline transmission. This feedback can

occur, because both the laser and the cavity mirrors are aligned to the same optical axis. Therefore, light reflected of the first cavity mirror is fed back into the laser's cavity.

This effect was observed in previous diode-laser CRD experiments with Fabry-Pérot cavities, for example by [6]. Several explanations for this kind of cavity feedback exist, a good overview is given in [25, pp. 184–189].

We theorized that this feedback could be explained by a model of two coupled cavities. The first cavity in this model is the one between the laser's HR back facet and the first ring-down cavity mirror, while the second cavity is the ring-down cavity itself. If this model is correct, length matching the cavity lengths (i.e., matching the FSR of both cavities) should yield optimal feedback.

To further investigate this feedback behavior, the delay line (a hollow roof retroreflector on a mechanical stage) is used. When varying the length near the matching length (several millimeters) we observe a behavior that seemed to exhibit a periodicity with length rather than a clear maximum at equal cavity lengths. The resonances seem to change in shape periodically with length tuning, where short, pronounced peaks alternate with more stable resonance patterns.

3.2.3 Intracavity Gas Absorption

As can be seen from (32), gas absorption would affect the estimation of mirror reflectance if it is not excluded (e.g., by evacuating the cavity) or accounted for separately. Since an estimation for the absorption in ambient air is not feasible in the laboratory environment, the cavity is flooded with nitrogen for all ring-down measurements presented in 3.2.4.

For that purpose, a PVC tube of $\approx$ 25 mm diameter and a length slightly shorter than the distance d is inserted between the mirrors CMS1032 and CMS1033. This tube is flooded with high-purity nitrogen gas (Air Liquide ALPHAGAZ 1 Nitrogen) through a single valve in the middle of the tube. The gas flux into the cavity is controlled by a pressure-reducing valve mounted directly on the gas cylinder. As can be seen in Figure 8 an increase in Finesse (according to (51) and (52), corresponding to a higher ring-down time and lower intracavity losses) with higher gas pressures on the pressure-reducing valve, i.e. higher flux. However, above a threshold pressure well below 0.1 bar, no further increase in finesse could be measured. Therefore, all

ring-down measurements were conducted with a pressure slightly above 0.1 bar to exclude any influence of ambient air. We further assume that this threshold corresponds with the tube being entirely flooded by nitrogen gas.

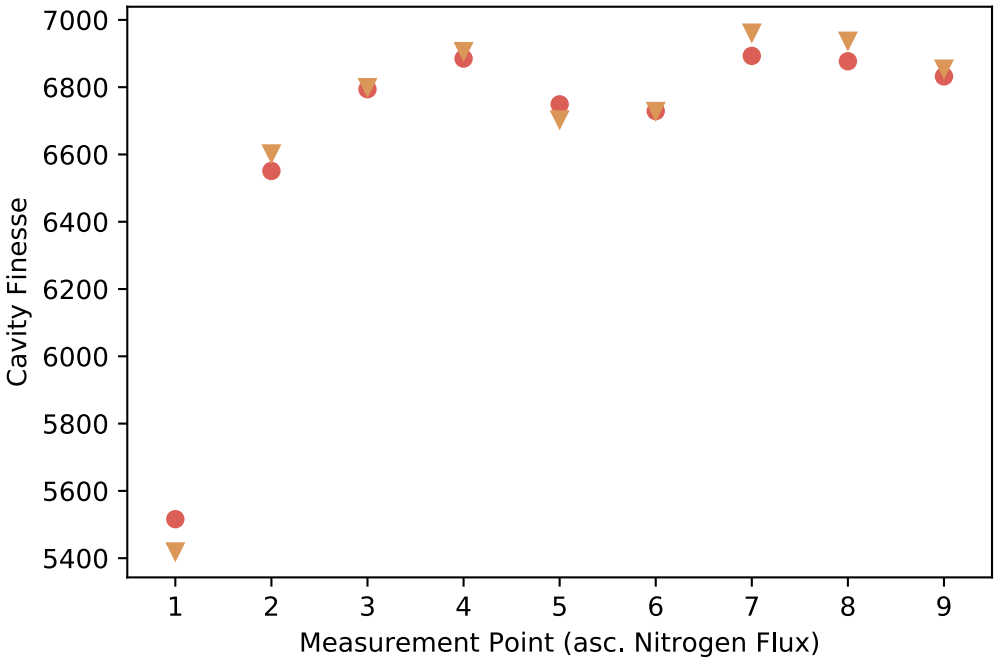

Figure 8: Influence of purging the measurement cavity with ppm level purity N_2 gas. At each pressure level on the pressure-reducing valve, i.e. each level of gas flux into the cavity, two measurements were performed (orange triangles and red dots). While the pressure strictly increases from measurement 1 to measurement 9, the coarse scale of the manometer only allowed to measure distinct pressure values for points 7, 8, and 9, which were recorded at 0.1 bar, 0.2 bar and 0.3 bar respectively. As can be seen from the plot, a threshold is reached well below 0.1 bar.

Based on this assumption, we can estimate the absorption coefficient $\alpha(\lambda)$. For this purpose, the absorption spectrum for a gas cell of length 92 cm filled according to the gas manufacturer's specifications (see A 4) was simulated in the relevant spectral region (Temperature 296 K, pressure 1 atm, using data from HITRAN2016 [26]). The resulting absorption curve for the entire spectral region is shown in Figure 9. From that we can conclude that the contribution of gas absorption to the measured ring-down time, according to (32) and (52), is less than 25 ppm at all measurement points.

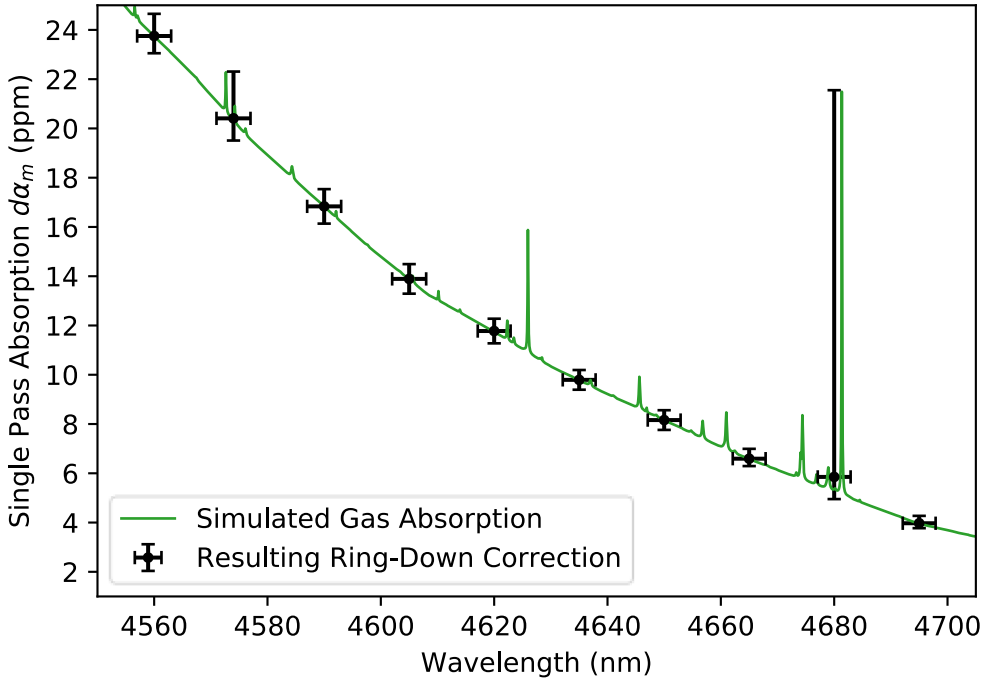

Figure 9: Calculated gas absorption (green curve) and the resulting corrections for our ring-down measurements (black dots). As can be seen, the vertical error interval is given by the extreme values of the absorption in the interval defined by the (horizontal) wavelength band.

To estimate absorption for the respective ring-down measurements presented in 3.2.4, in detail, the following procedure was employed: First, the bandpass of the reflection grating monochromator at the measurement wavelength was calculated according to the manufacturer's specifications.[5] Secondly, the gas absorption spectrum for the interval defined by this bandpass was taken. Thirdly, the mean over the interval was calculated. Lastly, both the minimum and maximum absorption value in this spectral interval were taken as the lower and upper bound of an error estimation. This allows for a correction of the ring-down reflectance measurements by the contribution of gas absorption as well as an estimate of the systematic error introduced by this method of reducing absorption.

Table 1 gives the complete set of calculated values for the wavelengths at which ring-down measurements are taken. Note that the extrema given represent a

[5] This bandpass is almost identical to the spectral interval defined by the wavelength error bars given in Table 2. However, the error bars also account for an additional uncertainty of ± 0.7 nm due to limited precision and accuracy of the employed monochromator.

maximum error estimation, as absorption values for all possible spectral light intensity distributions are within the given bounds.

Table 1: Calculated values for the effect of gas absorption at the wavelengths where ring-down measurements were performed (compare 3.2.4)

Wavelength λ (nm)	Mean Gas absorption $d\alpha_m$ (ppm)
4560.0 ± 3.0	$23.8^{+0.9}_{-0.7}$
4574.0 ± 2.9	$20.4^{+1.9}_{-0.9}$
4590.0 ± 2.9	$16.8^{+0.7}_{-0.7}$
4605.0 ± 2.9	$13.9^{+0.6}_{-0.6}$
4620.0 ± 2.9	$11.8^{+0.5}_{-0.5}$
4635.0 ± 2.9	$9.8^{+0.4}_{-0.4}$
4650.0 ± 2.9	$8.2^{+0.4}_{-0.4}$
4665.0 ± 2.8	$6.6^{+0.4}_{-0.3}$
4680.0 ± 2.8	$5.9^{+15.7}_{-0.9}$
4695.0 ± 2.8	$4.0^{+0.3}_{-0.2}$

3.2.4 Experimental Data and Results

The reflectance measurements are performed in close succession with the procedure being as follows: First the cavity is aligned to maximum transmission with the monochromator in zero order, i.e. without wavelength filtering. This involves the adjustment of the ring-down cavity mirrors, the delay stage, and modifying the laser diode current. Then, the monochromator is set to the desired wavelength. At this wavelength the signal is optimized again (solely by aligning the cavity mirrors). Then, several averaged ring-down traces were recorded at each wavelength (256 averages per trace, 16–32 traces). A single exponential model, according to (53), was fitted to each individual averaged trace, resulting in a series of measured values for the ring-down time $\tau(\lambda)$. To exclude any influence of shut-off processes and setup response time on the obtained results, we excluded the first 2.5 µs of each ringdown signal in the process of fitting. This approach is illustrated in Figure 10, where averaged ring-down measurement curves for each wavelength are shown.

As can be seen in Figure 11, these measurements exhibit a very high repeatability. From the measurement series depicted in Figure 11, we calculated the statistical mean and uncertainty for each $\tau(\lambda)$, which are given in Table 2. These values were successively converted to finesse and reflectance values according to (51). Finally, by (52) and allowing for the corrections according to wavelength in Table 1, the

mean total loss $\bar{L}$ per mirror was derived. An overview of these values and their respective propagated uncertainties is given in Table 2.

Table 2: Overview of the CRD measurement results. The uncertainty in τ results from the statistical variance of the measurement series alone. It is given as the $\pm 1\sigma$ standard error of the mean of the individual measurement series shown in Figure 11.

λ (nm)	τ (µs)	$\mathcal{F}$	$\bar{L}$ (ppm) per mirror
4560.0 ± 3.7	15.17 ± 0.18	15530 ± 180	$178.5^{+3.3}_{-3.1}$
4574.0 ± 3.7	14.200 ± 0.047	14536 ± 51	$195.7^{+2.7}_{-1.7}$
4590.0 ± 3.7	12.725 ± 0.021	13027 ± 26	$224.3^{+1.2}_{-1.2}$
4605.0 ± 3.7	10.449 ± 0.050	10696 ± 52	$279.8^{+2.1}_{-2.1}$
4620.0 ± 3.6	8.327 ± 0.037	8525 ± 39	$356.7^{+2.2}_{-2.2}$
4635.0 ± 3.6	6.070 ± 0.026	6214 ± 28	$495.8^{+2.7}_{-2.7}$
4650.0 ± 3.6	4.1624 ± 0.0065	4261.1 ± 8.1	$729.1^{+1.8}_{-1.8}$
4665.0 ± 3.6	2.9779 ± 0.0069	3048.5 ± 7.8	$1023.9^{+3.1}_{-3.0}$
4680.0 ± 3.6	1.6394 ± 0.0022	1678.3 ± 2.9	$1866.1^{+18.9}_{-4.1}$
4695.0 ± 3.6	0.9833 ± 0.0023	1006.7 ± 2.6	$3116.8^{+8.3}_{-8.2}$

Subsequently, a best-fit curve was calculated for the gas absorption-corrected CRD data. It follows from (32) and (52) that the resulting reflectance data corresponds to the mean mirror reflectance $\bar{R}$ of CMS1032 and CMS1033. Therefore, the CRD data and its best-fit are compared to the 'mean mirror' model (derived in 3.1.2) in Figure 12. As can be seen from that diagram, the CRD measurements are in good agreement with the model derived from FTIRS.

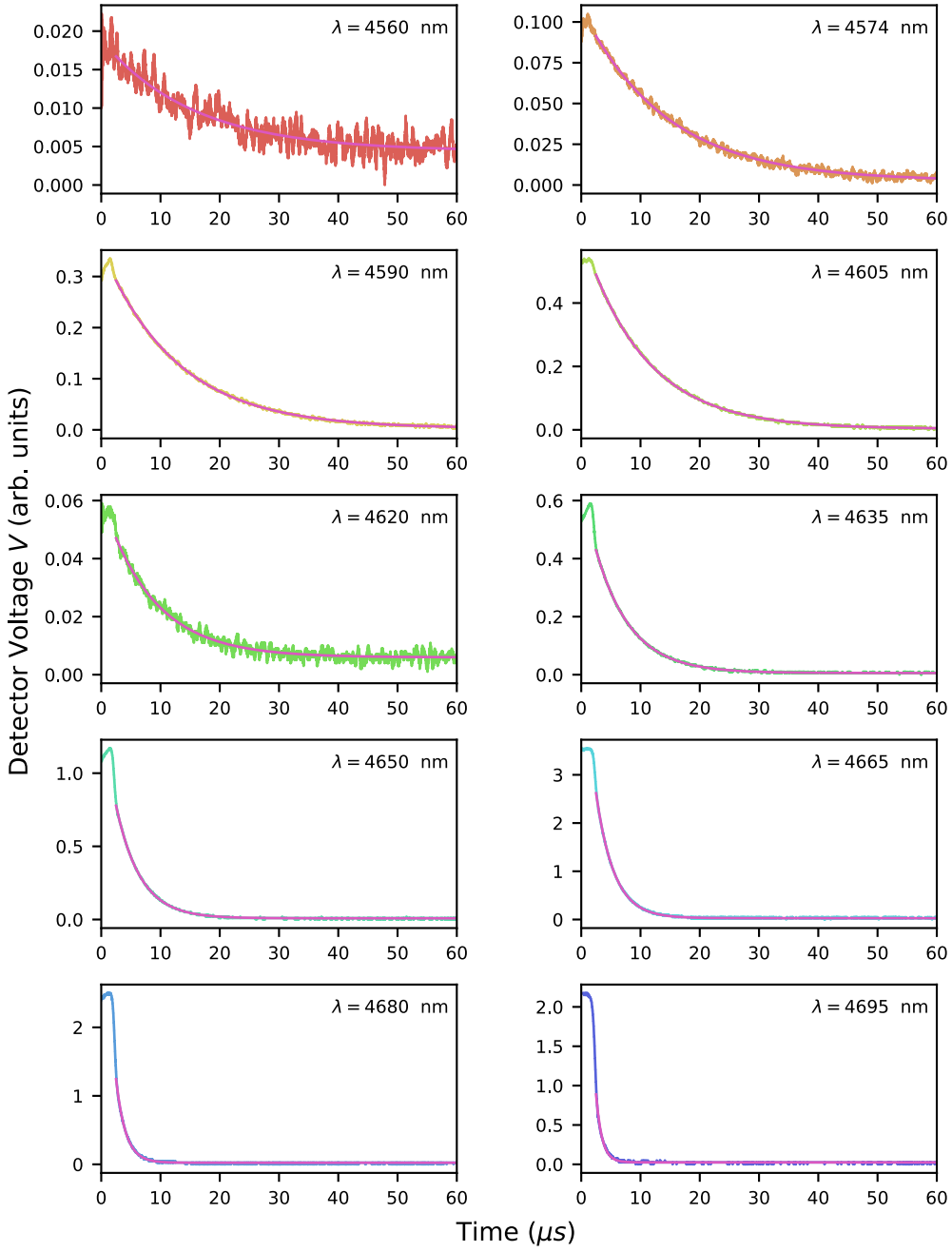

Figure 10: Typical ring-down curves per measurement wavelength (color according to wavelength) and according best-fit exponential curves (pink line). The best-fit curve is shown only in the range where the measurement data could be used. For times $t < 2.5$ µs both, the setup response time and switch-off effects in the QCL source influenced the recorded signal. The varying signal-to-noise ratio is due to the spectral power density of the QCL source (see A 2.1).

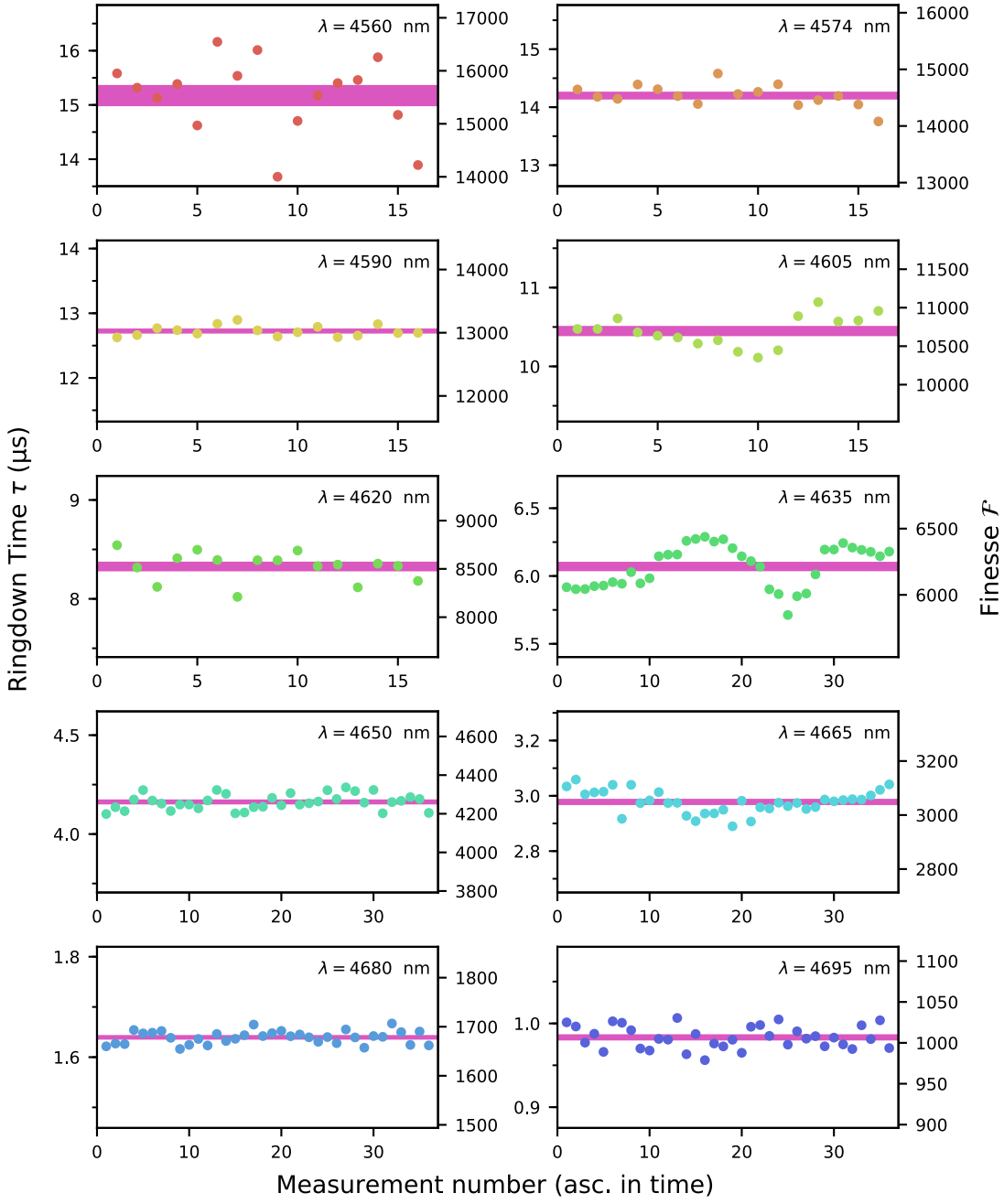

Figure 11: CRD measurement results. The colored dots each depict a single value for the ring-down time $\tau(\lambda)$, resulting from a best fit to single measured oscilloscope traces with 256 averages. Also shown in each plot is the mean ring-down time $\bar{\tau}(\lambda)$ (dark pink line), resulting from these measurements, and the respective $\pm 1\sigma$ standard error of the mean interval (light pink bar). These results are also given in Table 2. The left-hand ordinate gives the τ value, while the right ordinate gives the corresponding finesse $\mathcal{F}$; note that the axis increment was varied to better visualize variation.

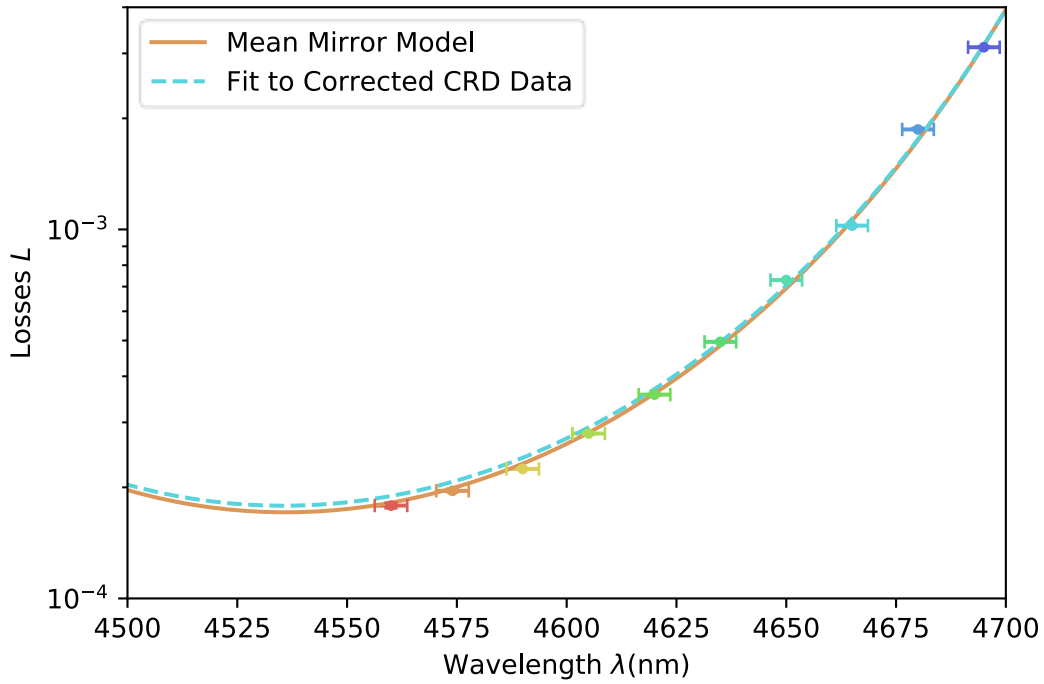

Figure 12: Comparison of the CRD results and the 'mean mirror' model developed in 3.1.2. Shown are the corrected mean loss data points (colored dots, according to Table 2), the best fit to this data (dashed blue line) and the mean mirror model (solid orange line). The ordinate error bars are mostly too small to be visible, refer to Table 2 for exact values.

Note that the FTIRS model did not include residual loss l (i.e., $L = T$; or $A + S = l = 0$ was assumed) due to the reasons mentioned in 3.1.1. Therefore, it is expected, that CRD measurements yield a slightly lower reflectance than the 'mean mirror' model. According to our best-fit model to the CRD data, the minimum mean single mirror losses are given by

$$\bar{L}\left(\lambda_{\text{center}} = 4535\,\text{nm}\right) \approx 178.4\,\text{ppm}$$

for the tested mirror pair, which is only 7.2 ppm higher than the optimal value derived from the FTIRS mode. Additionally, the mirror's center wavelength of $\lambda_{\text{center}} = 4535$ nm is in excellent agreement with the 4536 nm expected from 3.1.2.

An independent measurement of transmittance T, as described in 3.3, allows for another consistency check. Furthermore, if $\bar{R}$ and T are known, we can give an estimation for the residual loss l.

3.3 Transmittance Measurements

In addition to the reflectance measurements presented in 3.2, transmittance measurements at several wavelengths were performed. As presented in 3.3.1, the approach involved a direct transmittance measurement with lock-in detection (in contrast to a scheme by [27], measuring transmittance directly in a CRD setup). The data obtained from these measurements is presented and analyzed in 3.3.2

3.3.1 Experimental Setup

For the transmittance measurements, we used a direct measurement approach with a white light source and a single mirror. An indirect approach, as in [27], where transmittance is derived from a measurement of incoming, transmitted, and reflected power of a cavity, is not feasible in our case. This is due to two major reasons: On the one hand, our laser exhibited a broadband spectrum (see A 2.1), making it impossible to determine at which exact wavelengths light was coupled into the cavity; on the other hand, the feedback described in 3.2.2, all power measurements fluctuated heavily with time.

Therefore, we opted for a direct transmission measurement apparatus as shown in Figure 13. The underlying principle is to measure light intensity impinging on the detector (TL PDA20H-EC) both with and without the crystalline supermirror sample (same mirror type as described in 3.1) in the light path, resulting in measurement values for I_{trans} and I_{tot}, respectively. By then dividing these two quantities, one obtains the transmittance $T = I_{\mathrm{trans}}/I_{\mathrm{tot}}$. The approach is feasible because the transmittance is expected to be above 150 ppm in all cases.

For the apparatus, a globar type white light source (TL SLS203L/M, see A 2.2) was favored over using the QCL source from 3.2. The advantages of this approach are the inherent stability of the thermal source paired with its superior spectral range coverage. In fact, the spectral range had to be limited using an narrow optical bandpass filter (Spectrogon NB-4515-090, see A 5) to avoid problems with higher-order diffraction in the monochromator (Spectral Products CM110, see A 3). The passband of the filter was tuned by tilting and heating.[6]

[6] Heating was achieved by placing the filter in the filter holder of the globar light source.

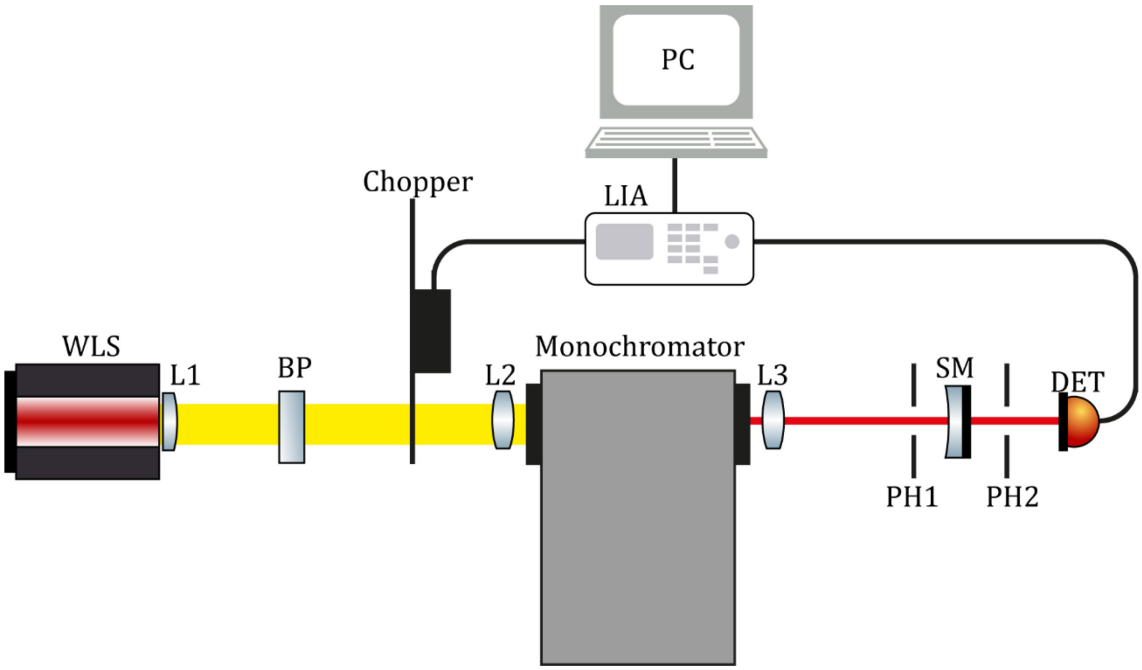

Figure 13: Schematic of the direct transmission measurement setup. A white light source (WLS) is collimated by a lens (L1), then spectrally filtered by an optical bandpass filter (BP). The light is then chopped by a mechanical chopper wheel, focused by a lens (L1) on the monochromator entrance slit. After spectral filtering by means of the monochromator, the light is recollimated by a lens (L2). The intensity with and without sample mirror (SM) is measured by a photodiode detector (DET). Stray light is minimized by two iris diaphragms ('pinholes', PH1/PH2) and lens tubes (not depicted). The detector is connected to a lock-in amplifier (LIA), which also controls the chopper frequency. (Illustration created with component library three by Alexander Franzen)

One major drawback of the thermal source, however, is its low spectral power density. Measuring transmittances well below 0.05% therefore requires the use of a lock-in amplifier (Stanford Research Systems SR810 DSP) and longer integration time per measurement. Since a lock-in amplifier can only be used to enhance a periodic signal, the light beam was modulated using a mechanical chopper wheel (TL MC2000B-EC). As indicated in the schematic in Figure 13, the chopper frequency was controlled by the internal reference signal generator of the lock-in amplifier. The signal of the lock-in amplifier was recorded via PC for data processing. This lock-in measurement scheme allowed for both, a higher signal-to-noise ratio and a higher dynamic range of the apparatus.

The chopping of the light beam, as well as multiple reflections in the setup, led to significant stray light. Therefore, lens tubes and iris diaphragms ('pin holes') were introduced to the apparatus. This suppressed the stray light to a satisfactory extent.

For all data points presented in 3.3.2, the lock-in internal reference signal was set to 180 Hz. The following procedure was used: First, the monochromator was adjusted

to the desired wavelength. If necessary, the optical filter was adjusted accordingly at this point. Secondly, a reference measurement without the mirror was done, resulting in a measurement value for $V_{\mathrm{tot}} \propto I_{\mathrm{tot}}$. Thirdly, the mirror was placed in the beam path and a measurement of $V_{\mathrm{trans}} \propto I_{\mathrm{trans}}$ was performed. Finally, the obtained data points were averaged, resulting in a mean value for the transmittance $T(\lambda)$ at each measurement wavelength.

3.3.2 Experimental Data and Results

For the transmittance measurements, a single mirror, as described in 3.1, was used. The resulting data is shown in Table 1. It is of note, that the absolute uncertainty of V_{tot} is comparable to that of V_{trans}. Since V_{tot} is more than four orders of magnitude higher than V_{trans}, the error is therefore negligible. As a result, the uncertainty of our transmission measurements is dominated by the error in the measurement of V_{trans}. This error was estimated to be 10% based on the evaluation of the measurement series, resulting in the uncertainties shown in Table 3.

Table 3: Direct transmission measurement results. Listed are the wavelength λ at which measurements were taken, the total input power equivalent voltage V_{tot}, the transmitted power equivalent voltage V_{trans} and the resulting transmittance $T = V_{\mathrm{trans}}/V_{\mathrm{tot}}$. The uncertainty of V_{tot} is negligible and therefore omitted.

λ (nm)	V_{tot} (mV)	V_{trans} (µV)	T (ppm)
4450.0 ± 3.8	44.85	14.28 ± 1.43	319 ± 32
4475.0 ± 3.8	33.90	6.83 ± 0.69	201 ± 21
4500.0 ± 3.8	61.82	11.23 ± 1.13	182 ± 19
4525.0 ± 3.7	61.31	9.40 ± 0.94	153 ± 16
4550.0 ± 3.7	56.33	8.00 ± 0.80	142 ± 15
4575.0 ± 3.7	44.34	7.91 ± 0.80	178 ± 18
4600.0 ± 3.7	15.38	3.87 ± 0.39	251 ± 26

In contrast to the measurements in 3.2, these results can be compared directly to the best-fit model for the FTIRS of mirror CMS1032. This comparison is depicted in Figure 14, where the transmittance measurement data, a best-fit to the data, and the FTIRS fit for CMS1032 are shown.

As can be seen, the center wavelength of our best-fit model to transmission measurements of $\lambda_{\mathrm{center,trans}} = (4532.1 \pm 2.1)$ nm is shifted towards lower wavelengths when compared to FTIRS data in 3.1.1. This shift of approximately 8.3 nm is likely caused by errors in the transmittance measurements. As this deviation is, however,

in the same range as the variation between coatings of the same coating run (see the comparison of CMS1032 and CMS1033 in 3.1.1), the transmittance data obtained by our measurements remains significant.

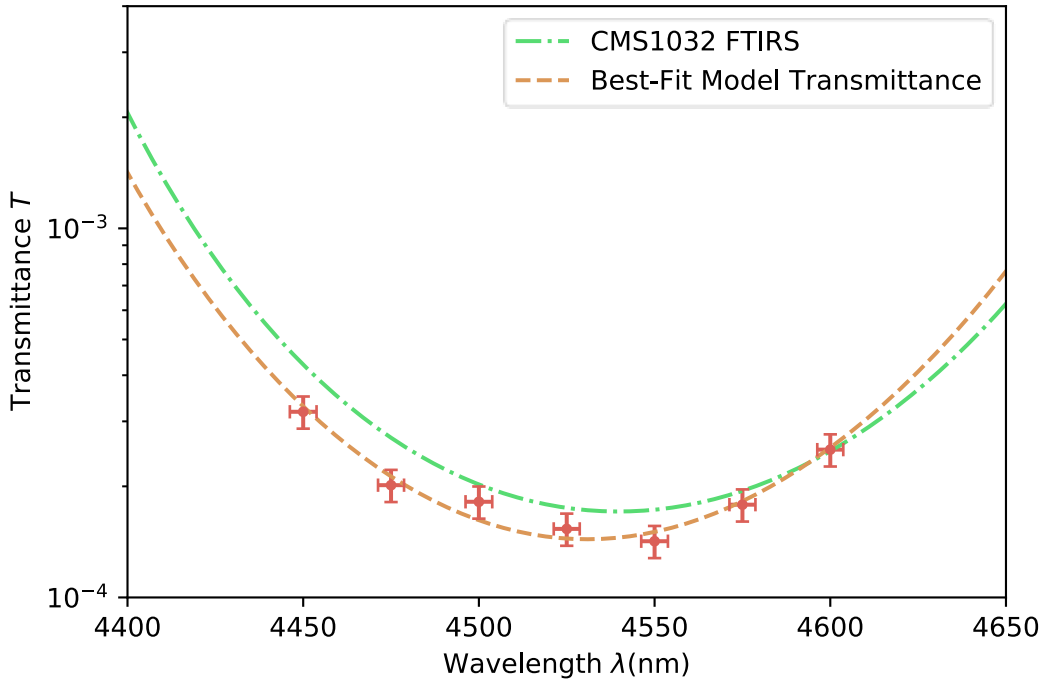

Figure 14: Comparison of the transmittance measurement data (red dots) and a best-fit curve (orange dashed line) to the best fit to FTIRS measurements of CMS1032 (green dash-dotted line). While the lower transmittance is expected due to residual loss l in the coatings, the shift of the stopband center is attributed to measurement uncertainty.

3.4 Discussion

Since both the CRD measurements in 3.2 and the transmittance measurements in 3.3 yielded mutually confirming results, we can estimate the expected residual loss l for crystalline substrate-transferred supermirror coatings to be in the range of $l_{est} \approx (37 \pm 18)$ ppm range at the stopband center. However, this estimate is of limited accuracy due to following reasons.

First, ring-down measurements were conducted with a mirror pair, while transmittance measurements were performed on a single mirror. While both results were expected and shown to be within less than 0.5% difference in stopband center wavelength λ_{center}, we effectively compared a 'mean mirror' and a single mirror loss and transmittance curve. This will lead to small deviations compared to a direct absorption measurement.

Secondly, a nitrogen gas of higher purity should be used in future experiments. While the intracavity gas absorption correction, as realized in 3.2.3, is an acceptable approach, gas cylinder manufacturers tend to inaccurately specify residual trace gasses in ppm-purity gasses. This is less the case for ppb-level purity products. Therefore, higher purity gas would lead to a more accurate model, as gas absorption could be calculated more precisely. It would, however, not result in significantly lower intracavity gas absorption, as the lion's share of absorption is already caused by nitrogen itself.

Thirdly, the validity of the results obtained by the presented nitrogen-purging method needs to be confirmed. This should best be done by conducting similar measurements in vacuum.

Lastly, the transmittance measurements should be systemized further. While our measurement principle will work for transmittances lower than 100 ppm, it would be favorable for the measurement uncertainty to improve several parts of the apparatus. Some possible improvements are: the use a monochromator grating blazed closer to the mirror stopband wavelength, resulting in higher optical intensities; the use of a lowpass optical filter instead of a bandpass filter, also resulting in higher transmission; the use of advanced detection technology, obtaining a better signal-to-noise ratio, especially when measuring transmitted optical power $I_{\mathrm{trans}} \propto V_{\mathrm{trans}}$.

4 Conclusion and Outlook

All measurements conducted in course of the thesis can be considered a success with regards to the aims in 1.2. While CRD measurements, presented in 3.2, yielded results comparable in accuracy to much more expensive measurement approaches, e.g. [8]. We further demonstrated that our rather simple direct transmission measurement approach is feasible for transmittances > 100 ppm with an error of 10%.

The results obtained demonstrate the potential of our cost-effective apparatus. While the CRD measurements yielded a maximum reflectance of $\bar{R} = \left(0.9998215^{+(31)}_{-(33)}\right)$, the minimum transmittance was determined to be $T = (142 \pm 15)$ ppm. This allowed for an estimation of residual loss, in the order of $l = (37 \pm 18)$ ppm.

This result also demonstrates that the relatively novel technique of substrate-transferred supermirrors is already on par with the specifications of established physical vapor deposition mirror coatings (e.g. the mirror pair used in [28]).[7] As the mirrors used for the thesis at hand were the first of its kind at a wavelength above 4 µm, our results clearly illustrate the potential of substrate-transferred crystalline coatings.

Moreover, our measurements have shown, that the assumption of 'equal mirrors', often made when determining mirror reflectance via the CRD method (e.g. by [8], [27]), is questionable. It would therefore be best practice to characterize three mirrors at a time, if available and feasible. Otherwise, at least a 'mean mirror' fit model, as demonstrated in 3.1.2, should be used instead of a single mirror transfer matrix model.

Although the used mirrors performed very well in our setup, further investigative effort should be put in the exact determination of mirror birefringence in substrate-transferred crystalline coatings. Previous estimates [8], [20] suggest, that

[7] It is of note that we conducted a small number of comparison measurements on a pair of vapor-deposition mirrors. These results indicate that their quality varies greatly, often yielding results far worse than the specified reflectance. However, this observation needs to be confirmed by systematic measurements.

birefringence is significantly higher when compared to state-of-the-art (vapor deposition technology) supermirrors [28]. In principle, the setup used by Fleisher et.al. [28] could be adapted for that purpose with little effort.

Lastly, we noticed that accurate measurements and/or models for the refractive index of AlGaAs with a high fraction of AlAs are not available to date. While accurate measurements were conducted for AlAs ratios in $Al_xGa_{1-x}As$ up to $x = 0.804$ [29], and an advanced model based on these measurements exists [30], there is no published data available for higher AlAs fractions, forcing researchers to use an older, less accurate model.

Symbols and Abbreviations

Symbols

%	percent (10^{-2})
ppm	parts per million (10^{-6})
τ	cavity ring-down time, cavity decay time
$\bar{x}$	arithmetic mean of a series of measurements for a quantity x
σ	standard error of the mean
R	reflectance
L	total mirror loss (i.e., $L = T + A + S = T + l$)
T	transmittance
l	residual loss (i.e., $l = A + S$)

Abbreviations

CMS	Crystalline Mirror Solutions
CRD	cavity ring-down
FTIRS	Fourier Transform Infrared Spectrometer
FWHM	full width at half maximum
ICL	interband cascade laser
MIR	mid-infrared
NIR	near-infrared
QCL	quantum cascade laser
ROC	radius of curvature
TEC	thermoelectric cooling
TEM	transverse electro-magnetic
TL	Thorlabs
VIS	Visible

Figures and Tables

Figures

Tables

References

[1] D. Z. Anderson, J. C. Frisch, and C. S. Masser, "Mirror reflectometer based on optical cavity decay time," *Appl. Opt.*, vol. 23, no. 8, p. 1238, 1984.

[2] J. M. Herbelin *et al.*, "Sensitive measurement of photon lifetime and true reflectances in an optical cavity by a phase-shift method," *Appl. Opt.*, vol. 19, no. 1, p. 144, 1980.

[3] A. O'Keefe and D. A. G. Deacon, "Cavity ring-down optical spectrometer for absorption measurements using pulsed laser sources," *Rev. Sci. Instrum.*, vol. 59, no. 12, pp. 2544–2551, 1988.

[4] D. Romanini, I. Ventrillard, G. Méjean, J. Morville, and E. Kerstel, "Introduction to Cavity Enhanced Absorption Spectroscopy," in *Cavity-Enhanced Spectroscopy and Sensing*, vol. 179, G. Gagliardi and H.-P. Loock, Eds. Heidelberg: Springer, 2014, pp. 1–60.

[5] Y. Gong and B. Li, "High-reflectivity measurement with a broadband diode laser based cavity ring-down technique," *Appl. Phys. B Lasers Opt.*, vol. 88, no. 3, pp. 477–482, 2007.

[6] Y. Gong, B. Li, and Y. Han, "Optical feedback cavity ring-down technique for accurate measurement of ultra-high reflectivity," *Appl. Phys. B Lasers Opt.*, vol. 93, no. 2–3, pp. 355–360, 2008.

[7] T. K. Zhao, Z. C. Qu, Y. L. Han, and B. C. Li, "Two optical feedback schemes for cavity ring-down technique for high reflectivity measurements," *Chinese Phys. Lett.*, vol. 27, no. 10, 2010.

[8] G. D. Cole *et al.*, "High-performance near- and mid-infrared crystalline coatings," *Optica*, vol. 3, no. 6, 2016.

[9] F. Adler, K. C. Cossel, M. J. Thorpe, I. Hartl, M. E. Fermann, and J. Ye, "Phase-stabilized, 1.5 W frequency comb at 2.8–4.8 μm," *Opt. Lett.*, vol. 43, no. 9, pp. 1330–1332, 2009.

[10] K. F. Renk, *Basics of Laser Physics. For Students of Science and Engineering*, 2nd ed. Cham: Springer International Publishing, 2017.

[11] B. E. A. Saleh and M. C. Teich, *Fundamentals of Photonics*, 1st ed. New York: John Wiley & Sons, 1991.

[12] B. E. A. Saleh and M. C. Teich, *Fundamentals of Photonics*, 2nd ed. Hoboken: Wiley, 2007.

[13] H. Kogelnik and T. Li, "Laser beams and resonators," *Appl. Opt.*, vol. 54, no. 10, pp. 1550–1567, 1966.

[14] K. S. Thorne and R. D. Blandford, *Modern Classical Physics*. Princeton: Princeton University Press, 2017.

[15] I. Kimel and L. Elias, "Relations Between Hermite and Laguerre Gaussian Modes," *IEEE J. Quantum Electron.*, vol. 29, no. 9, pp. 2562–2567, 1993.

[16] K. K. Lehmann and D. Romanini, "The superposition principle and cavity ring-down spectroscopy," *J. Chem. Phys.*, vol. 105, no. 23, pp. 10263–10277, 1996.

[17] J. W. Rohlf, *Modern Physics from α to Z0*. New York: Wiley, 1994.

[18] Y. Gong and B. Li, "Effect of instrumental response time in exponential-decay-based cavity ring-down techniques for high reflectivity measurement," in *Laser-Induced Damage in Optical Materials*, 2007, vol. 6720, p. 67201E–1–67201E–8.

[19] S. J. Byrnes, "Multilayer optical calculations," pp. 1–20, 2018.

[20] G. D. Cole, W. Zhang, M. J. Martin, J. Ye, and M. Aspelmeyer, "Tenfold reduction of Brownian noise in high-reflectivity optical coatings," *Nat. Photonics*, vol. 7, no. 8, pp. 644–650, 2013.

[21] G. E. Jellison, "Optical functions of GaAs, GaP, and Ge determined by two-channel polarization modulation ellipsometry," *Opt. Mater. (Amst).*, vol. 1, no. 3, pp. 151–160, 1992.

[22] T. Skauli *et al.*, "Improved dispersion relations for GaAs and applications to nonlinear optics," *J. Appl. Phys.*, vol. 94, no. 10, pp. 6447–6455, 2003.

[23] D. Chandler-Horowitz and P. M. Amirtharaj, "High-accuracy, midinfrared ($450\text{cm}^{-1} \leqslant \omega \leqslant 4000\text{cm}^{-1}$) refractive index values of silicon," *J. Appl. Phys.*, vol.

97, no. 123526, pp. 1–8, 2005.

[24] C. Schinke, P. C. Peest, J. Schmidt, R. Brendel, K. Bothe, and M. R. Vogt, "Uncertainty analysis for the coefficient of band-to-band absorption of crystalline silicon," *AIP Adv.*, vol. 5, no. 067168, pp. 1–22, 2015.

[25] J. Morville, D. Romanini, and E. Kerstel, "Cavity Enhanced Absorption Spectroscopy with Optical Feedback," in *Cavity-Enhanced Spectroscopy and Sensing*, vol. 179, G. Gagliardi and H.-P. Loock, Eds. Heidelberg: Springer, 2014, pp. 163–209.

[26] I. E. Gordon *et al.*, "The HITRAN2016 molecular spectroscopic database," *J. Quant. Spectrosc. Radiat. Transf.*, vol. 203, pp. 3–69, Dec. 2017.

[27] C. J. Hood, H. J. Kimble, and J. Ye, "Characterization of high-finesse mirrors: Loss, phase shifts, and mode structure in an optical cavity," *Phys. Rev. A*, vol. 64, no. 3, p. 7, 2001.

[28] A. J. Fleisher, D. A. Long, Q. Liu, and J. T. Hodges, "Precision interferometric measurements of mirror birefringence in high-finesse optical resonators," *Phys. Rev. A*, vol. 93, no. 1, pp. 1–7, 2016.

[29] D. E. Aspnes, S. M. Kelso, R. A. Logan, and R. Bhat, "Optical properties of bulk Al x Ga 1– x As," *J. Appl. Phys.*, vol. 60, no. 2, pp. 754–767, 1986.

[30] S. Adachi, "Optical dispersion relations for GaP, GaAs, GaSb, InP, InAs, InSb, AlxGa1−xAs, and In1−xGaxAsyP1−y," *J. Appl. Phys.*, vol. 66, no. 12, pp. 6030–6040, 1989.

Appendix

A 1 Trigger Circuit Schematic

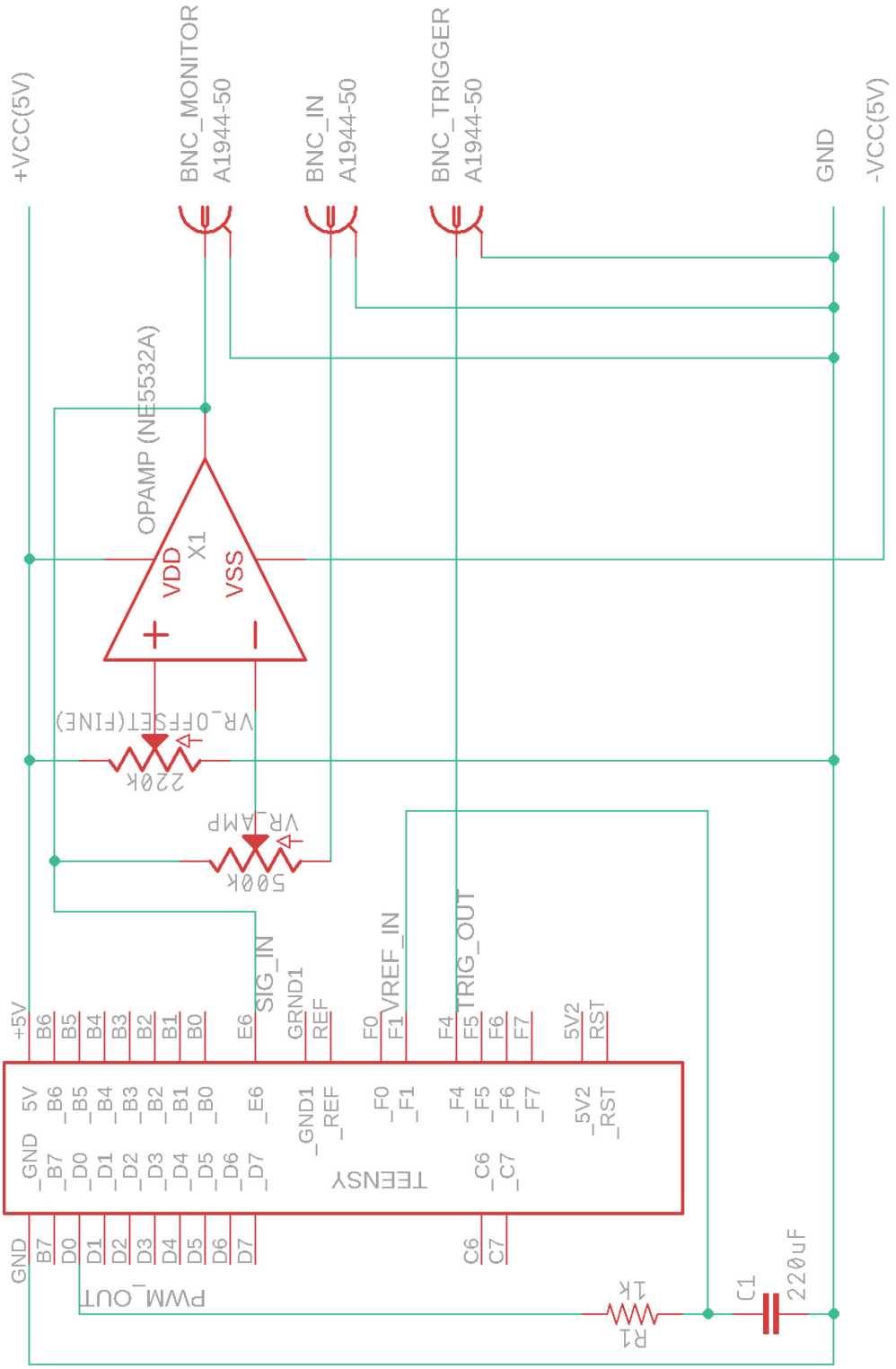

A 2 Data Sheets Thorlabs[8]

A 2.1 Fabry-Perot Quantum Cascade Laser (TL QF4550CM1)

	Symbol	Min	Typical	Max
Center Wavelength	λ_C	4.45 µm	4.55 µm	4.65 µm
Spectral Bandwidth (5% - 95% Integrated Power)	$\Delta\lambda$	-	130 nm	-
Output Power	P_{out}	450 mW	-	-
Operating Current	I_{pp}	-	900 mA	1100 mA
Threshold Current	I_{TH}	-	600 mA	-
Forward Voltage	V_F	-	10.5 V	12.0 V
Slope Efficiency	$\Delta P/\Delta I$	-	1.2 W/A	-
Divergence Angle, Parallel (FWHM)	$\theta_{\parallel}$	-	30°	-
Divergence Angle, Perpendicular (FWHM)	$\theta_{\perp}$	-	55°	-

Thorlabs reference QCL spectrum at operating current $I_{op} = 963.1$ mA[9]

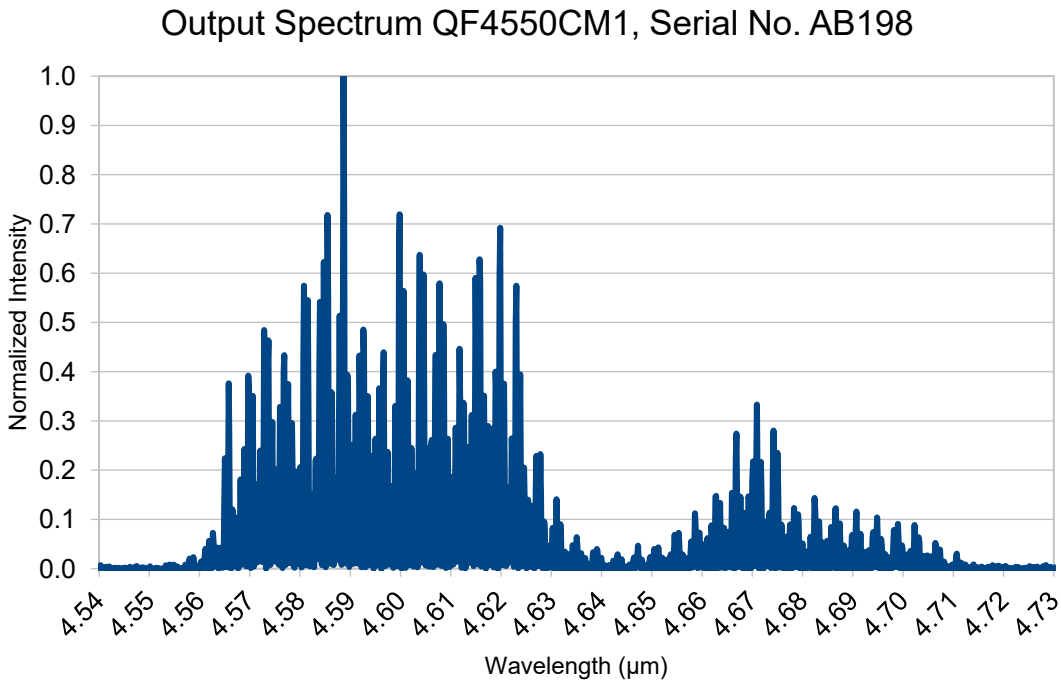

[8] If not stated otherwise, all data taken from PDF manuals found on the manufacturer's website for the respective products (https://www.thorlabs.com, 26.02.2019)

[9] Taken from documentation for the serial numbered diode used in this experiment. Provided upon delivery by the manufacturer.

A 2.2 Stabilized Free Space IR Light Source (TL SLS203L/M)

Specification	Value
Wavelength Range	500 – 9000 nm
Color Temperature	1500 K
Peak Wavelength	2400 nm
Color Temperature Stability	±15 K
Globar Power	24 W
Output Optical power [1]	>1.5 W
Globar Lifespan (Average)	10 000 hrs
Output Power Drift per Hour (Typical)	0.03%
Optical Power Drift per °C (Typical)	0.1%
Output Power stability [2]	<0.05%
Output Coupling	Free Space
Power Supply	90-264 VAC, 47-63 Hz
Operating Temperature	0 to 45 °C
Storage Temperature	-15 to 70 °C
Dimension (L x W x H)	209.1 mm × 55.0 mm x 57.5 mm (8.23" × 2.17" × 2.26")

Typical Spectrum

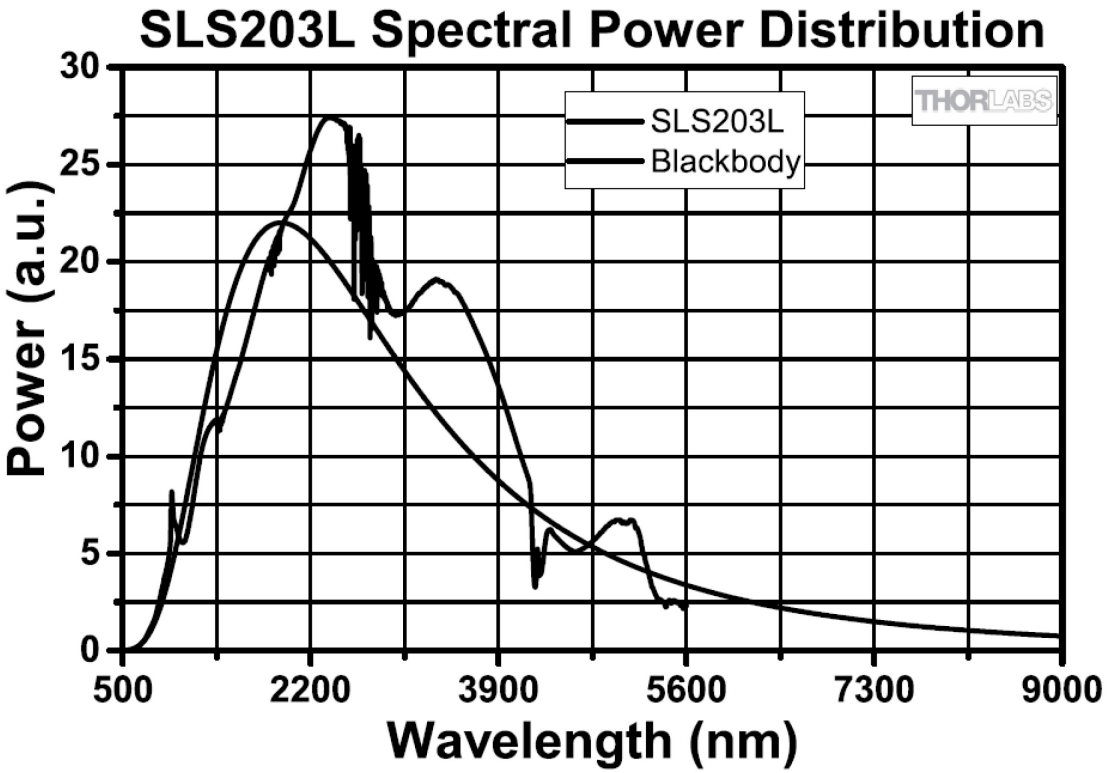

A 2.3 InAsSb Amplified Detector with TEC (TL PDA10PT-EC)

General Specifications[a]	
Optical Specifications	
Wavelength Range	1.0 – 5.8 µm
Peak Wavelength (λ_p)	4.9 µm
Peak Response (λ_p)	1.6 A/W (Typ.), 0.8 A/W (Min.)
Electrical Specifications	
Gain Adjustment Range	40 dB
Gain Steps	8
Gain Settings (dB)	0, 4, 10, 16, 22, 28, 34, 40
Filter Steps	8
Filter Settings (kHz)	12.5, 25, 50, 100, 200, 400, 800, 1600
Output Voltage[b]	
50 Ω	0 – 5 V
Hi-Z	0 – 10 V
Output Impedance	50 Ω
Max Output Current	100 mA
Load Impedance	50 Ω – Hi-Z
Offset [c]	20 mV (Typ.) 45 mV (Max.)
Offset Drift (40 dB)	2.7 mV/°C
TEC Temperature	-30 °C
Physical Specifications	
Detector	InAsSb
Active Area	Ø1 mm
Surface Depth	0.12" (3.1 mm)
Output	BNC
Package Size	3" x 2.2" x 2.2" (76.2 mm x 55.9 mm x 55.9 mm)
Weight (Detector/Power Supply)	0.42 lbs / 2.1 lbs (191 g / 955 g)
Power Supply	31 W
Input Power	100 – 120 VAC, 50 – 60 Hz (220 – 240 VAC –EC)
Storage Temperature	0 to 60 °C
Operating Temperature	0 to 30 °C

a. *All measurements performed with a 50 Ω load unless stated otherwise. The PDA10PT has a 50 Ω series terminator resistor (i.e., in series with amplifier output). This forms a voltage divider with any load impedance (e.g., 50 Ω load divides signal in half).*
b. *Saturation of the output voltage may cause damage to the InAsSb detector element.*
c. *After the temperature has stabilized on all gain steps. Also note that the worst-case offset is on the 40 dB gain step.*

A 3 Data Sheet Spectral Products CM110 Monochromator[10]

Design:	Czerny-Turner, dual-grating turrets
Focal Length:	110 mm
f/#:	3.9
Beam Path:	Straight through standard, right angle provided on request.
Wavelength Drive:	Worm and wheel with microprocessor control and anti-backlash gearing. Bi-directional. Usable in positive or negative grating orders.
Wavelength Precision:	0.2 nm
Wavelength Accuracy:	$\pm$0.6 nm
Slewing Speed:	$>$ 100 nm/s
Stray Light:	$< 10^{-5}$

[10] taken from the manufacturer's product website (https://www.spectralproducts.com/cm110.html, 26.02.2019)

A 4 Air Liquide Alpha Gaz Nitrogen 1 Purity Specifications

Gas Name	Molar Fraction
Nitrogen (N_2)	≥ 0.99999
Water (H_2O)	≤ 2 ppm
Oxygen (O_2)	≤ 2 ppm
Hydrocarbons (as CH_4)	≤ 0.2 ppm

A 5 Data Sheet Spectrogon Narrow Bandpass Optical Filter[11]

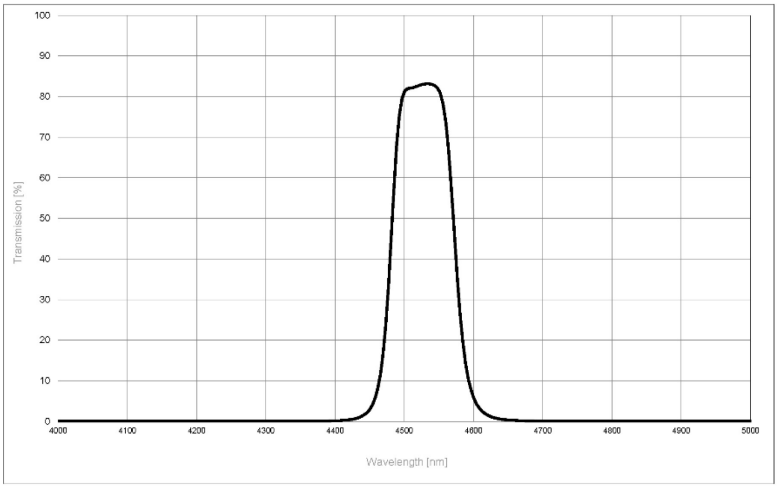

SPECTROGON
Optical filters • Coatings • Gratings

Date: 2018-06-13
Operator: SDZ

Article:
Art no: 713M10363
NB-4515-090 nm Ø25.4x1.0 mm

Specifications:
CWL: 4515 ±20 nm
HW: 90 ±20 nm
Tmin: 70 %
Blocking: 20 - 30000 nm (OD 3)

Measurement conditions:
Temperature: 23 °C
AOI: 0 deg

Measured values:
CWL = 4527,06 nm...OK
HW = 94,21 nm...OK
Cuton 5 % = 4456,31 nm
Cutoff 5 % = 4602,47 nm
HP1 = 4479,95 nm
HP2 = 4574,16 nm
Tpeak = 83,15 %...OK
Tavg = 81,57 %
Slope 1 = 0,72 %
Slope 2 = 0,84 %

Spectrogon:
Ref: T39769

Calibration traceable to NIST.
Spectrogon products conform in all aspects with the RoHS Directive.

[11] taken from the manufacturer's product site (http://www.spectrogon.com/wp-content/uploads/spectrogon/NB-4515-090-nm.pdf, 26.02.2019)

Abstract

The thesis at hand describes reflectance R and transmittance T measurements performed on a pair of substrate-transferred crystalline supermirrors centered at a wavelength of 4.54 µm. For this purpose, two low-cost, flexible and spectrally broadband measurement setups were built. For the reflectance measurements, a cavity ring-down scheme, using a Fabry-Pérot quantum cascade laser, was implemented. This setup exploited direct passive feedback effects of the measurement cavity on the source laser in a simple linear configuration. The transmittance was determined using a direct approach, comparing the intensity of both, the light incident on and the transmitted by the mirror coating; using a globar type white light source for power stability and lock-in detection to enhance the signal-to-noise ratio and dynamic range. In both setups, a reflection-grating monochromator was used to achieve spectrally resolved measurements. We measured a maximum reflectance $R = \left(0.9998215^{+(31)}_{-(33)}\right)$, and minimum transmittance $T = (142 \pm 15)$ ppm. Since $R + T + l = 1$, this allowed for an estimation of residual loss (absorption and scatter) in the order of $l = (37 \pm 18)$ ppm. Alongside these measurement results, the needed theoretical basics and models are derived and explained.

Zusammenfassung

Die vorliegende Arbeit beschreibt die Messung des Reflexionsvermögens R und des Transmissionsvermögens T, durchgeführt an zwei kristallinen Superspiegeln mit einer Zentralwellenlänge von 4.54 µm. Zu diesem Zweck wurden zwei kostengünstige, flexible und spektral breitbandige Messaufbauten erstellt. Für die Reflexionsmessungen wurde ein Cavity-Ringdown-Verfahren mit einem Fabry-Pérot-Quantenkaskadenlaser implementiert. Dieser Aufbau nutzte direkte passive Feedback-Effekte des Ringdown-Resonators auf den Quantenkaskadenlaser in einer einfachen linearen Anordnung. Das Transmissionsvermögen wurde unter Verwendung eines direkten Messansatzes bestimmt, wobei die Intensität, sowohl des einfallenden, als auch des von der Spiegelbeschichtung transmittierten Lichts verglichen wurde; dies unter Verwendung einer ‚Globar'-Weißlichtquelle zur Stabilisierung der Leistung einerseits, andererseits mit Hilfe eines Lock-In-Verstärkers um das Signal-Rausch-Verhältnis und den Dynamikbereich zu verbessern. In beiden Messaufbauten wurde ein Reflexionsgitter-Monochromator verwendet, um spektral aufgelöste Messungen zu ermöglichen. Wir haben ein maximales Reflexionsvermögen $R = \left(0.9998215^{+(31)}_{-(33)}\right)$ und ein minimales Transmissionsvermögen $T = (142 \pm 15)$ ppm gemessen. Da $R + T + l = 1$ gilt, konnte der Restverlust (Absorption und Streuung) in der Größenordnung von $l = (37 \pm 18)$ ppm bestimmt werden. Neben diesen Messergebnissen werden die benötigten theoretischen Grundlagen und Modelle abgeleitet und erläutert.